

# 1 Neutron-Neutron Correlations in the Photofission of U-238

2 J. Burggraf, D.S. Dale, and T. Forest  
3

4      *Department of Physics,*  
5      *Idaho State University, Pocatello, ID 83201*

6 G. Warren, S. Stave, S. Behling, and E. Church  
7

8      *Pacific Northwest National Laboratory, PO Box 999, Richland, Washington 99352*

(Dated: August 19, 2019)

9 **Background:** In the fission of actinides, the nearly back-to-back motion of the fission fragments has a strong  
10 effect on the kinematics of fission neutrons. This leads to a favoring of opening angles near  $0^\circ$  and  $180^\circ$  in the  
11 neutron-neutron (n-n) opening angle distributions of correlated neutron pairs from the same fission event.

12 **Purpose:** To measure the n-n opening angle and energy correlations in the photofission of  $^{238}\text{U}$ . As of this  
13 writing, measurements of correlated n-n opening angle distributions have been reported only for the spontaneous  
14 and neutron-induced fission of actinides. This work is the first to report such a measurement using photofission  
15 and will provide useful experimental input for photofission models used in codes such as MCNP and FREYA.

16 **Method:** Fission is induced using bremsstrahlung photons produced via a low duty factor, pulsed, linear electron  
17 accelerator. The bremsstrahlung photon beam impinges upon a  $^{238}\text{U}$  target that is surrounded by a large neutron  
18 scintillation detection system capable of measuring particle position and time of flight, from which n-n opening  
19 angle and energy are measured. Neutron-neutron angular correlations are determined by taking the ratio between  
20 a correlated neutron distribution and an uncorrelated neutron distribution formed by the pairing of neutrons pro-  
21 duced during different beam pulses. This analysis technique greatly diminishes effects due to detector efficiencies,  
22 acceptance, and experimental drifts.

23 **Results:** The angular correlation of neutrons from the photofission of  $^{238}\text{U}$  shows a high dependence on neutron  
24 energy as well as a dependence on the angle of the emitted neutrons with respect to the incoming photon beam.  
25 Angular correlations were also measured using neutrons from the spontaneous fission of  $^{252}\text{Cf}$ , showing good  
26 agreement with past measurements.

27 **Conclusions:** The measured angular correlations reflect the underlying back-to-back nature of the fission frag-  
28 ments. An anomalous decline in n-n yield was observed for opening angles near  $180^\circ$  for  $^{238}\text{U}$ .

## 29 CONTENTS

30 I. Overview of Neutron-Neutron Angular  
31 Correlations in Fission  
32    A. Theoretical Basis  
33    B. Past Measurements: Spontaneous and  
34       Neutron Induced Fission  
35    C. Considerations for Photofission

36 II. Experimental Setup  
37    A. Detectors  
38    B. Detector Shielding  
39    C. Bremsstrahlung Photon Beam  
40    D. DU Target  
41    E. Electronics

42 III. Measurement Techniques  
43    A. Particle Time of Flight and Energy  
44       Determination  
45    B. Particle Position Reconstruction  
46    C. Measurements with  $^{252}\text{Cf}$

47 IV. Analysis  
48    A. Cancelation of Detector Efficiencies, Drifts,  
49       and Geometric Phase Space  
50    B. Subtraction of Accidental Coincidences

## 51 V. Potential sources of error

52    A. Correlated versus uncorrelated n-n energy  
53       distribution  
54    B. Detector Cross-talk  
55       1. Simulation of Detector Cross-talk  
56       C. Neutron Scattering within the Target

## 57 VI. Results

58    A. Comparisons with FREYA  
59    B. Anomalous emission at large opening  
60       angles  
61       C. Considering  $\theta_{abs}$

## 62 VII. Concluding Remarks

## 63 VIII. Acknowledgments

## 64 References

## 65 I. OVERVIEW OF NEUTRON-NEUTRON 66 ANGULAR CORRELATIONS IN FISSION

67 The fission process is characterized by the emission of  
68 neutrons. Neutron emission in fission can be classified  
69 into two categories depending on the time of emission:

70 delayed and prompt. Prompt fission neutrons are de-  
 71 fined as neutrons that are emitted either immediately  
 72 after ( $< 10^{-14}$  seconds) fission, or during the scission  
 73 of the nucleus, and account for  $\sim 99\%$  of neutron emis-  
 74 sion [1]. Delayed neutrons are not relevant to the present  
 75 work because they account for only  $\sim 1\%$  of total neutron  
 76 emission in actinide photofission [1], and they are emit-  
 77 ted milliseconds to minutes after fission which is well out-  
 78 side the neutron acceptance timing window of the present  
 79 work.

80 Prompt fission neutron production occurs by means of  
 81 two distinct mechanisms. The dominant mechanism is  
 82 neutron emission from the fully accelerated fragments.  
 83 The second mechanism, referred to as *early* or *scission*  
 84 neutron emission, is the emission of neutrons during ei-  
 85 ther the scission of the nucleus or the acceleration of the  
 86 fission fragments. A large number of past studies have  
 87 established that the majority of prompt fission neutrons  
 88 (80%–98%) are emitted from the fully accelerated frag-  
 89 ments, while scission neutrons account for the remaining  
 90 2%–20% percent [2]. The nature of scission neutrons has  
 91 remained elusive since their first tentative observation in  
 92 1962 by Bowman *et al.* [3].

### A. Theoretical Basis

94 The neutron-neutron (n-n) opening angle distribution  
 95 of correlated neutron pairs, as seen in the lab frame, is  
 96 widely used for the quantification of n-n angular correla-  
 97 tions. Angular correlations in fission neutrons arise due  
 98 to the kinematics of the fission fragments. It has been  
 99 shown that neutrons released from the fully accelerated  
 100 fission fragments are evaporated isotropically in the frag-  
 101 ment's rest frame, and are emitted at speeds compara-  
 102 ble to that of the fragments themselves [4]. This leads  
 103 to the well-known U-shaped distribution in neutron-  
 104 neutron opening angle ( $\theta_{nn}$ ), which has been reported  
 105 in studies of neutron-induced, spontaneous, and in this  
 106 work, photofission.

107 The U-shaped distribution of  $\theta_{nn}$  can be understood  
 108 as the result of the boost provided to the neutrons by the  
 109 fission fragments in binary fission. Due to the conserva-  
 110 tion of momentum, the fully accelerated fission fragments  
 111 are traveling nearly back-to-back, and neutrons emitted  
 112 from different fragments are boosted in opposite direc-  
 113 tions, whereas neutrons emitted from the same fragment  
 114 are boosted in the same direction. Thus, because the  
 115 velocities of the fission fragments are large enough to ac-  
 116 count for a significant portion of the kinetic energy of  
 117 fission neutrons, neutron pairs emitted from the acceler-  
 118 ated fragments exhibit a favoring of opening angles near  
 119 0° if emitted from the same fragment and 180° if emitted  
 120 from different fragments, and consequently, a suppression  
 121 of opening angles near 90°.

122 The favoring of large and small n-n opening angles  
 123 shows a strong dependence on neutron energy. Neutrons  
 124 with higher energy are more likely to have been emit-

125 ted along the same direction as the fission fragments and  
 126 are therefore expected to favor large and small opening  
 127 angles. On the other hand, neutrons emitted with lower  
 128 energy are more susceptible to kinematical focusing along  
 129 the direction of the recoil of the emitting fragment. The  
 130  $\theta_{nn}$  distribution and its dependence on neutron energy  
 131 are expected to shed light on several fundamental aspects  
 132 of the fission process including the neutron multiplicity  
 133 distributions associated with the light and heavy fission  
 134 fragments, the nuclear temperatures of the fission frag-  
 135 ments, and the mass distribution of the fission fragments  
 136 as a function of energy released. In addition, the unique  
 137 kinematics of fission and the resulting n-n correlations  
 138 have the potential to be the basis for a new tool to char-  
 139 acterize fissionable materials [5].

### B. Past Measurements: Spontaneous and Neutron Induced Fission

142 The first measurement of the angular correlation  
 143 among coincident neutrons from fission was performed  
 144 by Debenedetti *et al.* [6] in 1948 from neutron induced  
 145 fission of  $^{235}\text{U}$ . The next measurement of this type was  
 146 performed by Pringle and Brooks in 1975 [7], in which  
 147 neutrons emitted from the spontaneous fission (SF) of  
 148  $^{252}\text{Cf}$  were found to have high coincidence rates at small  
 149 opening angles near 0° and large opening angles near  
 150 180°. In order to produce a result that is insensitive to  
 151 the effects of detector geometry and efficiency, the present  
 152 work uses techniques similar to those used in reference [7],  
 153 in which a ratio is taken between a correlated opening an-  
 154 gle distribution and an uncorrelated opening angle distri-  
 155 bution. Measurements of n-n angular correlation in the  
 156 SF of  $^{252}\text{Cf}$ , the most studied case of correlated neutron  
 157 emission in fission (see Refs. [7–10]), were also performed  
 158 in the present work and show good agreement with past  
 159 measurements, as seen in Fig. 1. Correlated n-n measure-  
 160 ments have also been performed using thermal neutron  
 161 induced fission of  $^{235}\text{U}$ ,  $^{233}\text{U}$ , and  $^{239}\text{Pu}$  [11], as well as  
 162 the SF of  $^{240}\text{Pu}$  [12].

### C. Considerations for Photofission

164 The photofission reaction occurs during the de-  
 165 excitation of a nucleus after the absorption of a pho-  
 166 ton. For photon energies between 6 and 25 MeV, this  
 167 absorption occurs primarily via the giant dipole reso-  
 168 nance (GDR) excitation. One distinct and useful as-  
 169 pect of photofission, relative to neutron-induced fission,  
 170 is the low transfer of angular momentum to the nucleus,  
 171 which gives rise to a simpler set of selection rules for  
 172 the transfer of angular momentum. For the photofis-  
 173 sion of even-even nuclei, excitation occurs primarily via  
 174 electric dipole transitions, and to a lesser extent electric  
 175 quadrupole transitions, which gives rise to anisotropies  
 176 in the fission fragment angular distribution that are far

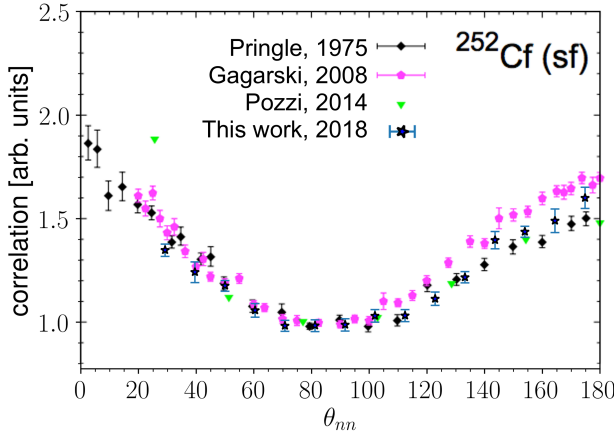


**FIG. 1:**  $\theta_{nn}$  distribution from the spontaneous fission of  $^{252}\text{Cf}$ . The minimum neutron energy cut-off for Pringle [7], Gagarski [10], and Pozzi [12] is 0.425 MeV, 0.425 MeV, and 0.7 MeV, respectively, and for this work is 0.4 MeV.

more pronounced than for other types of fission [13].  
 These anisotropies are expressed in the angular distribution of emitted neutrons. For these reasons, photofission is increasingly being used as a means to study sub-nuclear structures and the fundamentals of the fission process. Such studies are needed in order to dial in various model parameters required for an accurate theoretical description of the fission process.

## II. EXPERIMENTAL SETUP

This experiment was carried out at the Idaho Accelerator Center (IAC), using their short-pulsed linear accelerator, which is an L-band frequency (1300 MHz) electron linear accelerator. See section II C for the accelerator parameters used during the experiment. Figure 2 shows a top-down diagram of the experimental arrangement.

### A. Detectors

The detection system measures neutron position and time of flight (ToF), which is defined as the time taken for a particle to travel from the fission target to a detector. The purpose of the ToF measurement is to determine the kinetic energy of detected neutrons and to distinguish between photons and neutrons. The detection system's positional precision is  $\pm 9$  cm, which gives an average angular precision of  $\pm 6^\circ$  in opening angle reconstruction.

The detection system consists of fourteen shielded scintillators made from Polyvinyl Toluene (PVT) arranged in a ring around the target (see Figs. 2 and 3). Attached to both ends of each scintillator are 10-cm long, non-scintillating, ultra-violet transmitting, plastic light-guides. A Hamamatsu 580-17 photomultiplier (PMT) tube is fixed to each light-guide using optical glue. In or-

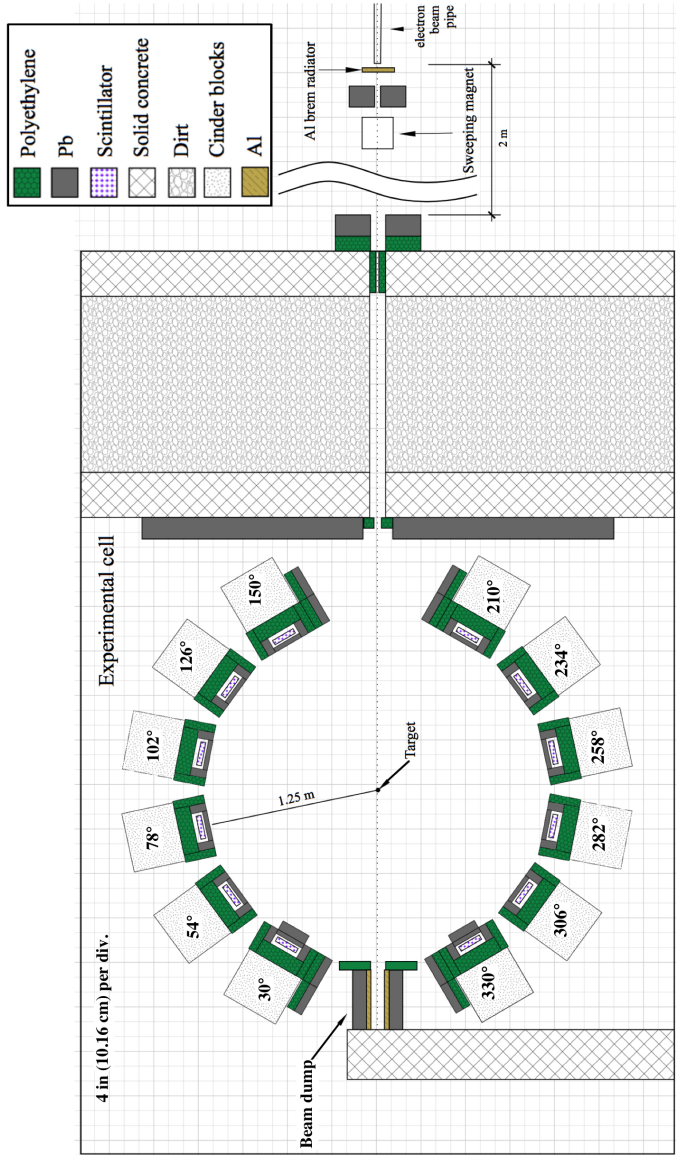


**FIG. 2:** To-scale, top down diagram of the experimental setup. An electron beam impinges upon a 3.8 cm thick Al radiator, and the resulting bremsstrahlung beam enters the experimental cell from the top of the figure. The supporting structure for each detector has been labeled according to the angle, in degrees, between the center of each detector and direction of the incoming photon beam. The fission target, a  $0.05 \times 2 \times 4 \text{ cm}^3$   $^{238}\text{U}$  cuboid, is rotated slowly about the vertical axis in order to mimic the effect of using a cylindrical target.

der to increase the chance that scintillation light remains inside the scintillator, the scintillators were polished to remove micro-imperfections and were then wrapped in reflective aluminized mylar.

Ten out of the fourteen scintillators had dimensions of  $76.2 \times 15.2 \times 3.8 \text{ cm}^3$ . The remaining four, the forward-most detectors located at  $\pm 30^\circ$  with respect to the beam, had dimensions of  $25.4 \times 15.2 \times 3.8 \text{ cm}^3$ . These scintilla-

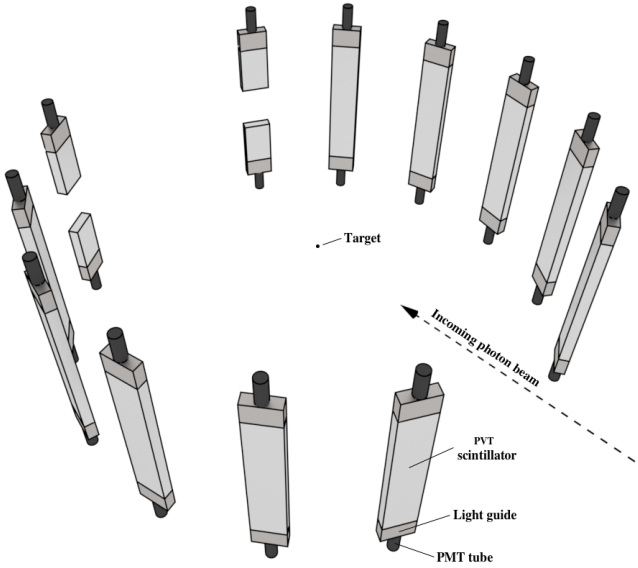


**FIG. 3:** 3-D rendering of the bare, unshielded scintillators, along with PMTs and light guides. Most of the open space between the scintillators was occupied by shielding, as seen in Fig. 2.

<sup>218</sup> tors, 1/3 the length of the rest, are the result of the  
<sup>219</sup> segmentation of two normally sized scintillators in order  
<sup>220</sup> to address the high photon flux at these locations caused  
<sup>221</sup> by the forward scattering of photons from the target.  
<sup>222</sup> Prior to segmentation, a photon was registered in the  
<sup>223</sup> forward-most detectors at a rate of about 0.9 photons  
<sup>224</sup> per pulse, and because the electronics were operated in  
<sup>225</sup> single hit mode (see section II E), this greatly reduced the  
<sup>226</sup> effective neutron detection efficiency. After segmentation  
<sup>227</sup> and optimization of shielding, the photon detection rate  
<sup>228</sup> was about 0.2 photons per pulse in each segmented de-  
<sup>229</sup>tector. The segmented detectors also differ from the rest  
<sup>230</sup> in that they were instrumented with only a single PMT,  
<sup>231</sup> and therefore provide a comparatively lower precision in  
<sup>232</sup> energy and position measurements. In order to test for  
<sup>233</sup> systematic errors that may have resulted from the use  
<sup>234</sup> of the segmented detectors, opening angle measurements  
<sup>235</sup> were compared with and without their use, and the dif-  
<sup>236</sup>ferences were well within experimental errors.

<sup>237</sup> The relative efficiencies of the neutron detectors as a  
<sup>238</sup> function of neutron energy and detector location were  
<sup>239</sup> calculated by dividing the measured by the known yields  
<sup>240</sup> of neutrons from the SF of  $^{252}\text{Cf}$ . The results are shown  
<sup>241</sup> in Fig. 4. Note that the effects of the uncertainty in  
<sup>242</sup> measured neutron energy (seen in Fig. 10) are folded into  
<sup>243</sup> this calculation. The analysis techniques described in  
<sup>244</sup> section IV are designed to eliminate the effects of detector  
<sup>245</sup> efficiency from the final result.

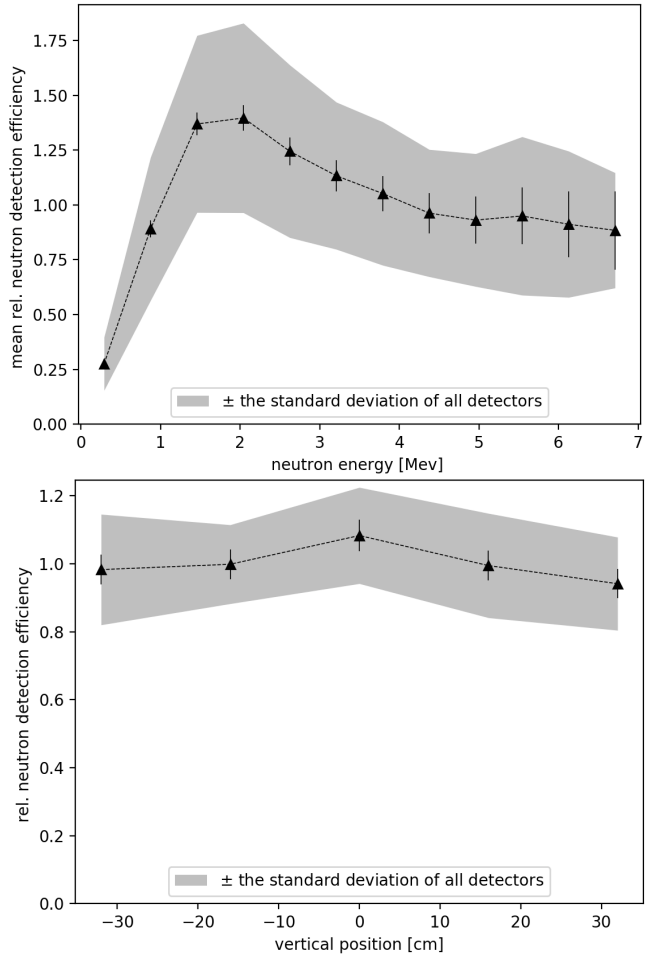


**FIG. 4:** (top) The mean relative neutron detection efficiency of all detectors as a function of neutron energy is calculated by dividing the measured energy distribution by the known energy distribution of neutrons from the SF of  $^{252}\text{Cf}$ . The relative efficiency differs from detector to detector, as demonstrated by the shaded region, which corresponds to the standard deviation of the relative efficiencies of all detectors. The error bars represent the uncertainty in the mean. (bot) Mean relative neutron detection efficiency as a function of the reconstructed position along the detectors longest axis.

## B. Detector Shielding

<sup>247</sup> The detector shielding, depicted in Fig. 5, was con-  
<sup>248</sup>structed using lead and polyethylene with the aim of re-  
<sup>249</sup>ducing detector cross-talk, the detection of photons, and  
<sup>250</sup>noise. The sides of each scintillator were shielded with 5  
<sup>251</sup>cm of lead followed by 5 cm of polyethylene to reduce the  
<sup>252</sup>chance of neutron cross-talk. Lead was not placed behind  
<sup>253</sup>the scintillators after an MCNP-POLIMI simulation in-  
<sup>254</sup>dicated that cross-talk would occur at significant rates  
<sup>255</sup>otherwise. Instead, 10 cm of polyethylene was placed be-  
<sup>256</sup>hind the scintillators. For a detailed discussion about the  
<sup>257</sup>issue of cross-talk, see section V B.

<sup>258</sup> The front face of each detector was subject to

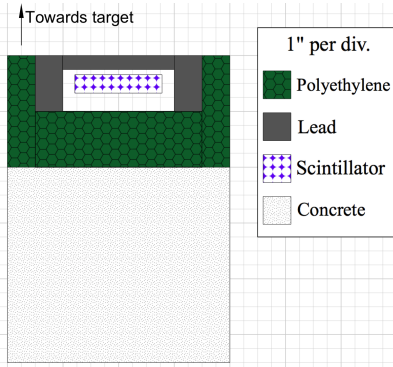


**FIG. 5:** Detector shielding was designed to reduce the detection of photons, room return, and detector cross-talk.

260 the highest photon flux due to the scattering of the  
 261 bremsstrahlung beam from the target. The detection of  
 262 a photon renders the given detector unable to detect any  
 263 subsequent fission neutrons from the same pulse due to  
 264 the detector recovery time. Lead mitigates this prob-  
 265 lem by reducing photon flux, but has the side effect of  
 266 scattering neutrons. If a neutron scatters prior to being  
 267 detected, the ToF measurement and position reconstruc-  
 268 tion are incorrect. The extent of measurement errors  
 269 caused by lead shielding were quantified using an MCNP  
 270 simulation, and, accordingly, 2.5 cm of lead was placed  
 271 along the front face of the detectors. This diminished  
 272 photon detection rates to reasonable levels, and, accord-  
 273 ing to the simulation, leads to a root-mean-square error  
 274 in opening angle and ToF of  $1^\circ$  and 0.3 ns, respectively,  
 275 due to neutron elastic scattering.

276 Because of the particularly high photon flux at the  
 277 sides of all detectors located directly adjacent to the  
 278 beam, an additional 2" of lead was placed along the sides  
 279 of these detectors. For the same reason, an additional 2"  
 280 of lead was also placed along the front faces of the de-  
 281 tectors farthest downstream, located at  $\pm 30^\circ$  from the  
 282 beam line. The differences in shielding design among the  
 283 detectors can be seen in Fig 2.

### 285 C. Bremsstrahlung Photon Beam

286 In order to ensure that all correlated neutrons pro-  
 287 duced are due to fission, the bremsstrahlung end-point  
 288 energy was set to 10.5 MeV, safely below the  $(\gamma, 2n)$   
 289 threshold of 11.28 MeV for  $^{238}\text{U}$ . Aluminum was chosen  
 290 for the bremsstrahlung radiator because it has a neu-  
 291 tron knockout threshold above the energy of the elec-  
 292 tron beam, which ensured that the radiator would not  
 293 be a source of fast neutrons with the potential to in-  
 294 terfere with the experiment. A sweeping magnet was  
 295 placed downstream from the bremsstrahlung radiator to  
 296 remove charged particles from the photon beam. Fol-  
 297 lowing the sweeping magnet, the beam traveled through  
 298 a series of polyethylene and lead collimators on its way

299 into the experimental cell in which the target was located  
 300 (see Fig. 2). Figure 6 shows the energy distribution of  
 301 photons that reach the target according to an MCNP  
 302 simulation that modeled the collimation and production  
 303 of the bremsstrahlung photons.

304 The electron beam pulse width was set to 3 ns at a  
 305 repetition rate of 240 Hz with a 1.1 A peak current. The  
 306 3 ns pulse width was small compared to the median neu-  
 307 tron ToF of 80 ns, and thus made a small contribution  
 308 to the uncertainty in the neutron energy determination.

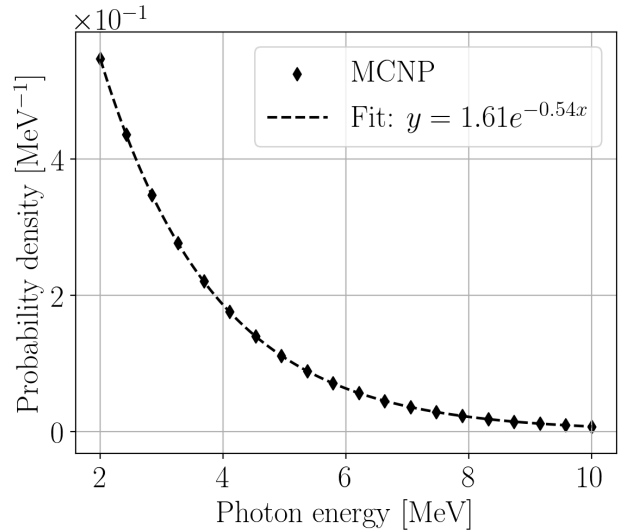


**FIG. 6:** MCNP simulation of the energy distribution of the bremsstrahlung photons that reach the fission target.  
 Photons with an energy below 2 MeV are excluded.

### 312 D. DU Target

313 A depleted uranium (DU) target in the shape of a thin  
 314 strip with dimensions of  $4 \times 2 \times 0.05 \text{ cm}^3$  and a mass of  
 315 7.6 g was used as the primary target.  $^{238}\text{U}$  was chosen as  
 316 the fission target because it is an even-even nucleus, and  
 317 as a consequence, the fission fragments are emitted with  
 318 a high degree of anisotropy with respect to the photon  
 319 beam direction [13].

320 Any target comprised of heavy nuclei has a significant  
 321 potential to scatter fission neutrons before they exit the  
 322 target. This is cause for concern, because neutrons that  
 323 scatter from heavy nuclei are likely to be deflected at  
 324 large angles, resulting in the measurement of  $\theta_{nn}$ 's uncon-  
 325 nected to the underlying fission kinematics. As discussed  
 326 in detail in section V C, an MCNP simulation estimated  
 327 that 6% of reconstructed  $\theta_{nn}$ 's are perturbed due to neu-  
 328 tron scattering within the  $^{238}\text{U}$  target. Moreover, it is  
 329 more likely that neutrons emitted along the wide, 2 cm,  
 330 axis of the  $^{238}\text{U}$  target undergo a scattering event than  
 331 neutrons emitted along the thinnest, 0.05 cm, axis. As  
 332 a result, detectors located collinear to the widest axis of

333 the target would see relatively fewer neutrons due to increased scattering along this axis. This bias is removed  
 334 by slowly rotating the target about the vertical axis during data acquisition at a rate of one rotation per 8 seconds.  
 335  
 336

338

### E. Electronics

339 A data acquisition system based on the NIM/VME standard was used. A schematic of the data acquisition logic is shown in Figure 7. The PMTs are supplied negative voltages ranging from 1300 to 1500 V by a LeCroy 340 1458 high voltage mainframe. Analog signals from the 341 PMTs were fed into a leading edge discriminator (CAEN 342 Mod. N841) with input thresholds ranging from 30 mV 343 to 50 mV. The threshold and supply voltages were 344 determined individually for each detector to minimize noise, 345 while simultaneously matching the efficiencies of all the 346 detectors as closely as possible. Logic signals from the 347 discriminator were converted to ECL logic and fed into a 348 CAEN model V1290A TDC. The timing of signals from 349 the PMTs were always measured relative to a signal from 350 the accelerator provided at the beginning of each pulse. 351 Even though a multi-hit TDC was used, only the first 352 signal in each pulse from any given PMT was taken into 353 account due to concerns over dead-time within the 354 electronics and signal reflections within the cables. On the 355 software side, the CODA 2.5 [14] software package de- 356 veloped by Jefferson Laboratory was used to read out the 357 data from the TDC and digitally store it for analysis.  
 358  
 359

361

## III. MEASUREMENT TECHNIQUES

362  
 363

### A. Particle Time of Flight and Energy Determination

364 The ToF of detected particles is used to distinguish 365 between neutrons and photons and to determine neutron 366 energy. A particle's reconstructed position is used to 367 determine direction of motion, which is then used to calculate 368 the opening angle between pairs of detected particles. 369 Position and ToF are each determined using the timing 370 of coincident signals from both PMTs of a given detector.

371 The sum of the times required for scintillation light 372 to travel from the point of scintillation to both PMTs 373 is equal to the time required for the light to travel the 374 full length of the scintillator, which is a constant for light 375 that travels parallel to the length of the scintillator. This 376 is supported by data, shown in Fig. 8, which were pro- 377 duced from a series of tests in which a collimated  $^{60}\text{Co}$  378 source was placed at seven different locations along a 379 scintillator. One of the two coincident photons emitted 380 by  $^{60}\text{Co}$  reaches the scintillator and the other is detected 381 by an auxiliary detector serving as the trigger. The pho- 382 tons incident on the scintillator have a spot size of less 383 than 1 cm due to source collimation. These events all

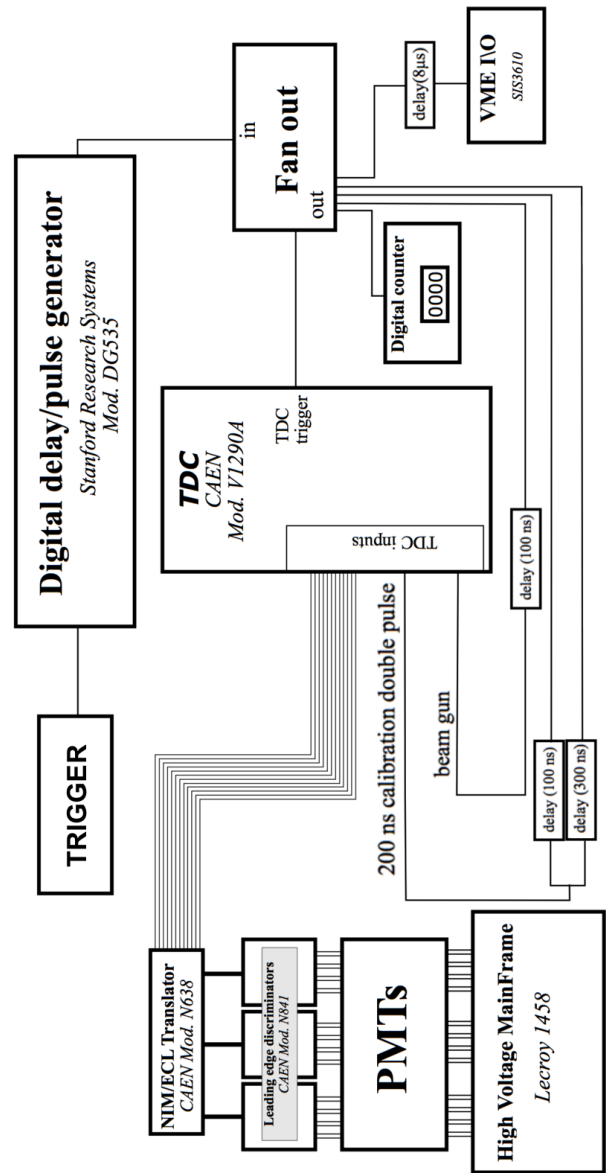
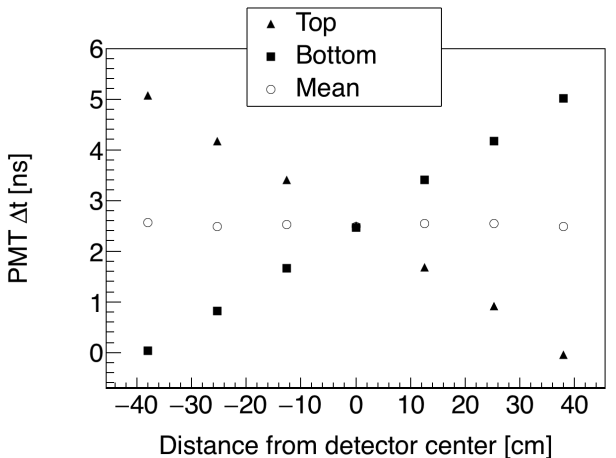


FIG. 7: Wiring diagram of the electronics setup.

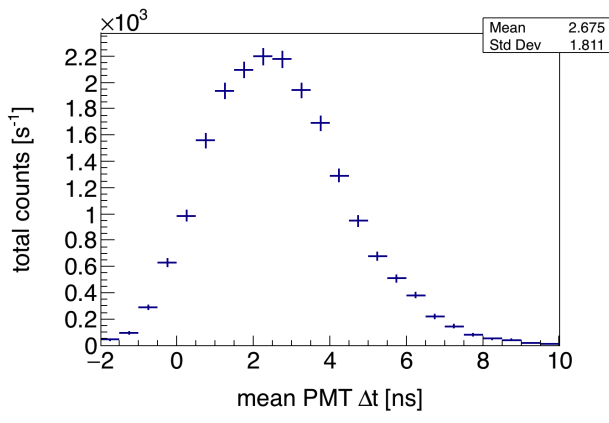
384 have equal transit time, regardless of the  $^{60}\text{Co}$  source's 385 position.

386 In Figure 8(a), it can be seen that the time required 387 for the scintillation light to propagate along the scintil- 388 lator has a large effect on the timing of each PMT alone, 389 however, the average of the times of both PMTs is a con- 390 stant, unaffected by the location at which the particle 391 undergoes scintillation. For this reason, taking the aver- 392 age of signals from two PMTs is advantageous because it 393 removes the roughly 5 ns timing error that would other- 394 wise exist due to the time required for scintillation light 395 to propagate along the scintillator. The requirement that 396 there be coincident events in both of a detector's PMTs 397 also aids in reducing noise.

398 During photofission measurements, ToF is calculated



(a)



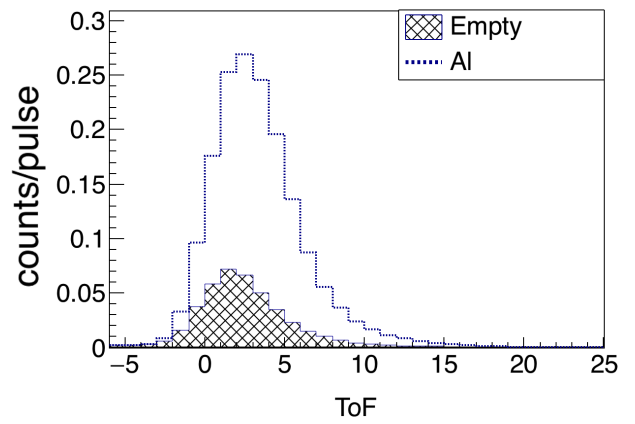
(b)

**FIG. 8:** A collimated  $^{60}\text{Co}$  source is used to produce photon events with constant ToF at seven locations along the detector.  $^{60}\text{Co}$  produces coincident photons, and one is detected by the scintillator and the other by a separate trigger detector.  $\Delta t$  is the timing of a PMT signal relative to a signal from the trigger detector. In (a), it can be seen that the average between signals from both PMTs does not depend on position. By using the PMT average, there is a reduction in error due to the time required for scintillation light to travel along the scintillator. The uncertainty in ToF measurements is equal to the standard deviation seen in (b), or about  $\pm 2$  ns, because all photons from the  $^{60}\text{Co}$  source have the same ToF.

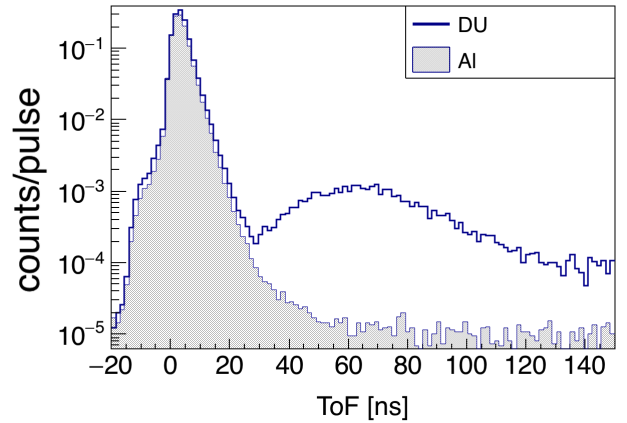
400 by the following expression:

$$\text{ToF} = t_{\text{mean}}^{\text{PMT}s} - t_{\text{beam}} + C, \quad (1)$$

401 where  $t_{\text{mean}}^{\text{PMT}s}$  is the mean of the times of signals from  
402 both PMTs of a scintillator,  $t_{\text{beam}}$  is the time of a sig-  
403 nal provided by the accelerator at the beginning of each  
404 pulse, and  $C$  is a constant timing offset. Any process that  
405 produces a timing delay that does not change from pulse  
406 to pulse contributes to  $C$ . For example, the time required  
407 for photons to travel from the bremsstrahlung radiator to  
408 the target, the propagation of signals through the cables



(a)



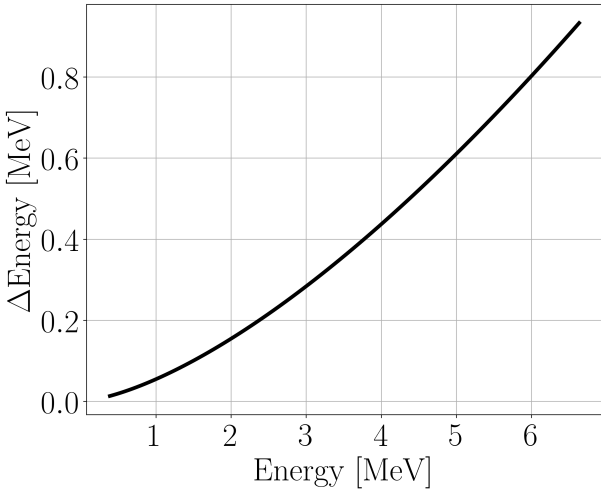
(b)

**FIG. 9:** (a) Comparison between the ToF spectrum of a non-neutron producing target made from Al, to the ToF spectrum produced when no target is used. The large increase in events around 4 ns is due to photons that scatter from the Al target. When no target is in place, sources of the peak seen here is used to find the timing offsets that make it so  $t = 0$  corresponds to the moment of fission. (b) Comparison between the Al and DU targets show a pronounced increase in events for DU between 35 and 130 ns due to the introduction of neutrons.

409 connecting the PMTs, delays in the electronics, etc.

410 The value of  $C$ , which may be different for each de-  
411 tector, is determined by comparing the timing spectra  
412 of the gamma flash produced by a non-neutron produc-  
413 ing aluminum target, to that produced when no target  
414 is used (see Fig. 9). The difference between these two  
415 spectra reveals a prominent peak in the ToF spectrum  
416 due to photons that scatter from the aluminum target.  
417 These photons must travel 125 cm to reach the center of  
418 any detector and 130 cm to reach the top, for which it  
419 takes light 4.2 ns and 4.3 ns to travel, respectively. The  
420 value of  $C$  used for each detector is equal to the value  
421 that places the time corresponding to the peak of the  
422 target-induced gamma flash at 4 ns.

423 The kinetic energy of a detected neutron is determined



(a)

**FIG. 10:** Uncertainty in neutron energy measurements as a function of measured neutron energy.

straightforwardly from its velocity, which is determined from its ToF under the assumption that the neutron traveled directly from the target to the detectors unimpeded. According to a series of MCNP simulations examining the scattering of fission neutrons within detector shielding and the fission target, neutrons predominantly travel to the detectors unimpeded. These simulations are discussed in sections IID and II A.

Figure 10 shows the measurement uncertainty in neutron energy due to error in the ToF determination.

## B. Particle Position Reconstruction

Each detector is not capable of measuring the position of a detected particle along the axes parallel to its width (15.24 cm) or depth (3.81 cm), which contributes  $\pm 3^\circ$  to the total angular uncertainty. The position of a detected particle along the 76.2 cm length of the scintillator is calculated using the timing difference of signals from both of a detector's PMTs. Assuming that scintillation light travels from an initial point, let it be  $x$  cm from the center of a scintillator, to both PMTs at a velocity that is constant with respect to the scintillator's length-wise axis, then the difference between the times at which the light will reach each PMT ( $\Delta t^{PMTs}$ ) is given by:

$$\begin{aligned} \Delta t^{PMTs} &= t^{PMT_1} - t^{PMT_2} \\ &= \frac{(L/2 + x)n_{\text{eff}}}{c} - \frac{(L/2 - x)n_{\text{eff}}}{c} \\ &= 2x \frac{n_{\text{eff}}}{c}. \end{aligned} \quad (2)$$

Solving for  $x$  gives

$$x = \frac{c}{2n_{\text{eff}}} \Delta t^{PMTs}, \quad (3)$$

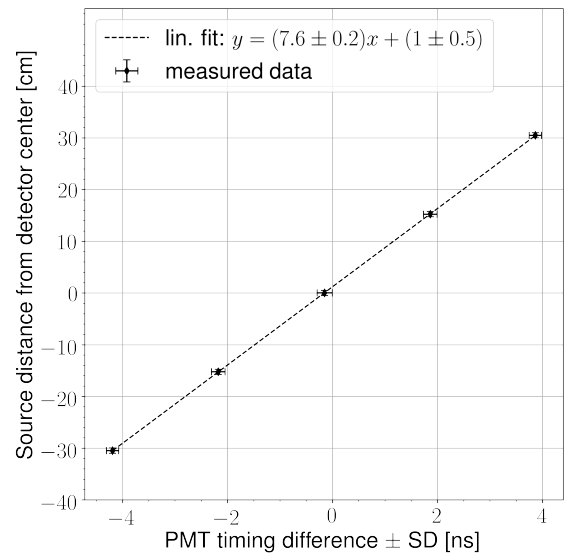


**FIG. 11:** A collimated  ${}^{60}\text{Co}$  source is used to produce photon events at five different positions along the scintillator. The mean PMT timing difference of events at each position varies linearly with respect to the distance of the  ${}^{60}\text{Co}$  source from the center of the detector. The result of a linear least squares fit to this data is used to calculate the position of detected particles along the length of each scintillator.

where  $t^{PMT_1}$  and  $t^{PMT_2}$  are the times of signals from each of a detector's PMTs relative to the accelerator gun pulse,  $L$  is the length of the scintillator,  $c$  is the speed of light,  $n_{\text{eff}}$  is the effective index of refraction of the scintillation material. A linear least squares fit between  $x$  and  $\Delta t^{PMTs}$  was performed on data gathered using coincident photons emitted by a collimated  ${}^{60}\text{Co}$  source, as described in the previous section. The resulting fit parameters, seen in Fig. 11, are used to find the position of detected particles.

Using the slope of the linear fit in Fig. 11, along with Eq. 3, an effective index of refraction of the scintillation material is calculated to be 2.0. This index of refraction is said to be “effective” because its measurement is sensitive only to the scintillation light’s average speed projected onto the axis parallel to the scintillator’s longest dimension, which is equal to the intrinsic speed of light in the material only if the light is traveling parallel to the scintillator’s length. While the detection of scintillation light by both PMTs favors light paths which are parallel or nearly-parallel to the scintillator’s length, there is some reflection of detected scintillation light from the boundaries of the scintillator. This effect contributes to the  $\pm 9$  cm measurement uncertainty in particle position reconstruction. As a result of these effects, the index of refraction measured here is  $\sim 25\%$  greater than the true value of the scintillation material.

477

### C. Measurements with $^{252}\text{Cf}$

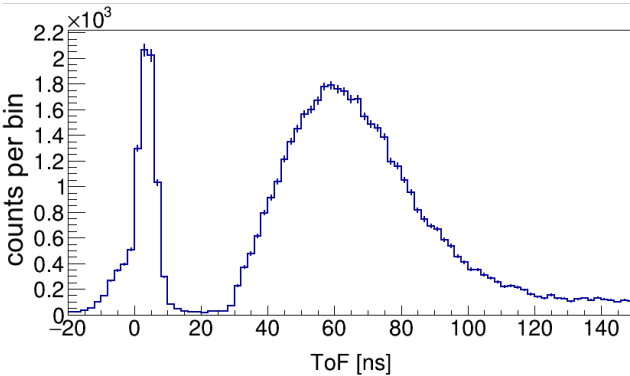


**FIG. 12:** Measured ToF spectrum from the SF of  $^{252}\text{Cf}$ . The sharp peak on the left is due to fission photons, followed by another peak due to fission neutrons.

A  $^{252}\text{Cf}$  source was placed at the center of the detection system shown in Fig. 2 in order to measure the n-n opening angle distribution. Several such past measurements have been performed (see Refs. [7–10]), and serve as a means to validate the methods used throughout this study.

The  $^{252}\text{Cf}$  source produces a cleaner ToF spectrum than photofission due to the lack of beam related backgrounds (see Fig. 12), and therefore these measurements have a better signal to noise ratio. Also, there is no concern over the detection of accidental neutron coincidences because the fission rate of the  $^{252}\text{Cf}$  source was about 3,500 fissions/s, making it highly unlikely that multiple fissions will occur during the electronic acceptance time window of 150 ns. The beginning of the 150 ns neutron acceptance time window was triggered by a 2-fold coincidence, within a 4 ns window, between two separate  $10 \times 10 \times 5 \text{ cm}^3$  plastic scintillators, one placed above and the other below the source at a distance of 30 cm. Aside from this difference in the time window triggering mechanism, identical methods were used for both photofission and SF measurements.

## IV. ANALYSIS

The efficiency and acceptance of the neutron detection system varies greatly over its opening angle range of  $20^\circ$  to  $180^\circ$ , as illustrated in Fig. 13. This is both due to the neutron detection system's non-spherical symmetry and to varying efficiency as a function of particle position on the detector. In order to give a result that is sensitive to angular correlations, but is highly insensitive to detector efficiencies and experimental drifts in PMT voltage, accelerator current, etc., the angular correlation is determined by dividing a correlated neutron distribution by

an uncorrelated neutron distribution. That is,

$$\text{angular correlation} = \frac{nn_{\text{corr}}(\theta)}{nn_{\text{uncorr}}(\theta)}, \quad (4)$$

where  $nn_{\text{corr}}(\theta)$  is the n-n yield after the subtraction of accidental n-n coincidences, and  $nn_{\text{uncorr}}(\theta)$  is a convolved distribution of uncorrelated n-n pairs, which is produced by pairing neutron events that occurred during different pulses. The subtraction of accidental n-n coincidences to produce  $nn_{\text{corr}}(\theta)$  amounts to a 10% correction, the procedure of which is covered in section IV B. The construction of  $nn_{\text{uncorr}}(\theta)$  is described in detail in section IV A.

**521 A. Cancelation of Detector Efficiencies, Drifts, and  
522 Geometric Phase Space**

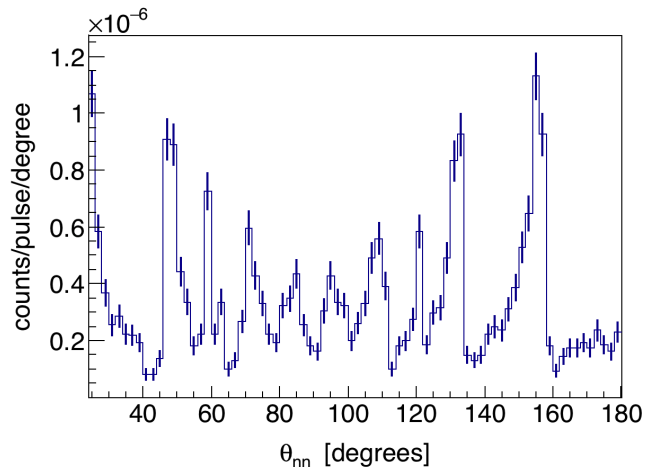


**FIG. 13:** Raw n-n opening angle yield from the photofission of  $^{238}\text{U}$ . This distribution is highly influenced by the detection system's geometric acceptance and efficiency.

The construction of  $nn_{\text{uncorr}}(\theta)$  is achieved by pairing detected neutrons that were produced during different accelerator pulses. The same set of pulses used for  $nn_{\text{corr}}(\theta)$  is used here, so each of these pulses individually consist of the detection of two coincident neutrons. When constructing  $nn_{\text{uncorr}}(\theta)$ , it is desirable that the neutrons comprising each uncorrelated n-n pair originated from different pulses that occurred as closely together in time as possible. A smaller time difference between pulses that are paired for this purpose increases the chance that both neutrons were detected under the same experimental conditions amid any drifting of accelerator current, PMT voltages, and varying rates of noise. However, some time difference between the pulses must be allowed so as not to cause insufficient counting statistics. Accordingly, uncorrelated n-n pairs used to construct  $nn_{\text{uncorr}}(\theta)$  are formed by neutrons that were detected within 30 minutes or less of each other.

Uncorrelated n-n pairs will have a slightly different joint energy distribution than correlated n-n pairs, which could affect the extent to which the effects of detector efficiency cancel in Eq. 4. This issue is addressed in section V A, where it is shown that these differences have little potential to significantly affect the final result.

Figure 14(a) shows the measured yield distribution of correlated neutrons,  $nn_{\text{corr}}(\theta)$ , from the photofission of  $^{238}\text{U}$ . The structure seen here is reflective of the underlying n-n angular correlations as well as the geometric acceptance and efficiencies of the neutron detectors. Figure 14(b) reveals how a clear picture of n-n angular correlations emerges when taking the ratio between  $nn_{\text{corr}}(\theta)$  and  $nn_{\text{uncorr}}(\theta)$ . Applying the same technique to a measurement of coincident neutrons from the photodisintegration of  $\text{D}_2\text{O}$  produces a flat line as expected (see Fig. 15)

## 558 B. Subtraction of Accidental Coincidences

The observation of two uncorrelated signals in the neutron ToF range, whether caused by neutrons, photons, or noise, is referred to as an *accidental coincidence*. Accidental coincidences due to noise and photons, which are estimated using a non-neutron producing aluminum target (see Fig. 16), amount to about 3% of all coincidences. Accidental coincidences due to neutrons are minimized by adjusting the accelerator's current so that there are, on average, less than 1.0 fissions per accelerator pulse. Nevertheless, statistical fluctuations in the number of fissions per pulse result in the production of accidental coincident neutrons that originated from different, and therefore, uncorrelated fissions. There are also accidental neutron coincidences caused by the occurrence of multiple  $(\gamma, n)$  reactions in a single pulse. The energy integrated  $(\gamma, n)$  cross-section of  $^{238}\text{U}$ , weighted by the bremsstrahlung energy distribution, is about a factor of 5.5 times greater than it is for photofission (see Fig. 17). As a result, the raw n-n coincident yield will contain a significant number of n-n coincidences from multiple  $(\gamma, n)$  reactions in relation to n-n coincidences from fission. The presence of accidental n-n coincidences has the effect of washing out the signal from correlated neutrons.

The raw measurement of n-n yield consists of a mix of correlated and accidental neutron coincidences, that is

$$584 \quad nn_{\text{raw}}(\theta_{nn}) = nn_{\text{corr}}(\theta_{nn}) + nn_{\text{acc}}(\theta_{nn}), \quad (5)$$

where  $nn_{\text{raw}}(\theta_{nn})$  and  $nn_{\text{acc}}(\theta_{nn})$  are the per-pulse n-n yields as a function of opening angle,  $\theta_{nn}$ , for all detected n-n pairs, and detected accidental n-n pairs, respectively. As already defined,  $nn_{\text{corr}}(\theta_{nn})$  is the per-pulse yield of detected correlated n-n pairs.

Because the n-n coincidences comprising  $nn_{\text{acc}}(\theta_{nn})$  consist of two independent detected neutrons, they are governed by the exact same physics and are subject to the exact same experimental conditions as n-n coinci-

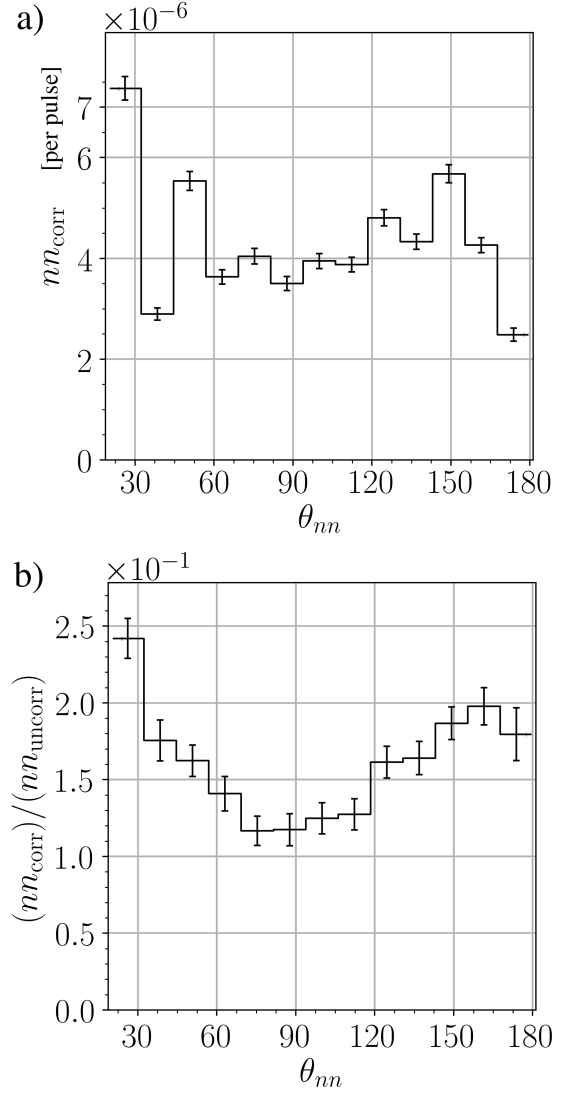


**FIG. 14:** n-n opening angle distribution from the photofission of  $^{238}\text{U}$  before the normalization procedure seen in Eq. 4 (a), and after normalization (b). All measured neutrons have an energy greater than 0.4 MeV.

dences formed by pairing of single neutrons that were detected during different pulses. Therefore, the opening angle distribution formed by pairing neutrons that were detected during different pulses, denoted  $nn_{dp}(\theta_{nn})$ , is proportional to  $nn_{\text{acc}}(\theta_{nn})$ .  $nn_{dp}(\theta_{nn})$  is constructed from the set of all possible pulse-pairs formed by pulses that occurred within 0.2 seconds of each other. The restriction in time difference is applied in order to increase the chance that pulse pairs together occurred under similar experimental conditions. There are no other restrictions on which pulses can be used in this case. Many pulse-pairs used for the construction of  $nn_{dp}(\theta_{nn})$  will

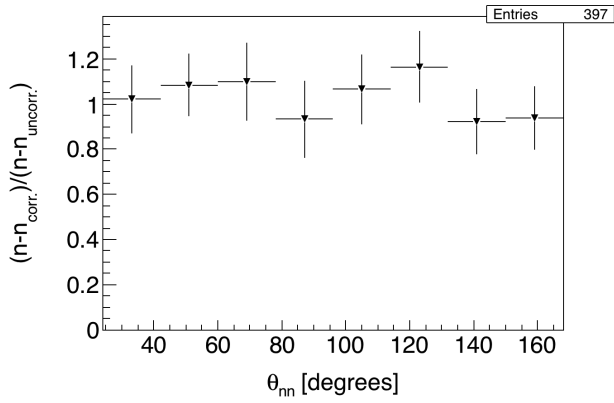


**FIG. 15:** A measurement of the angular correlation of uncorrelated neutrons emitted by the photodisintegration of  $\text{D}_2\text{O}$  gives the expected uniform distribution.

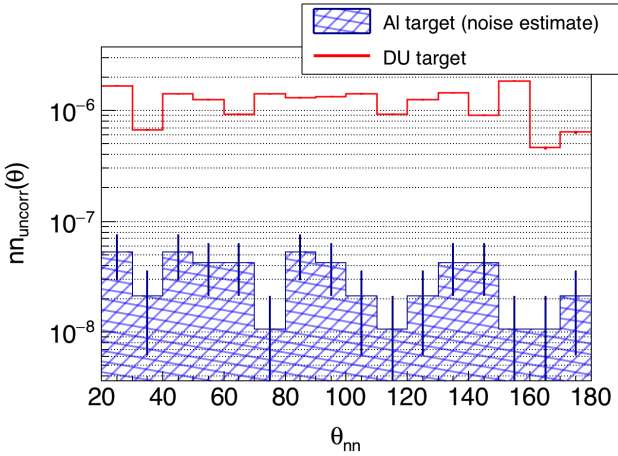


**FIG. 16:** An Al target was designed have the same thickness, in radiation lengths, as the  $^{238}\text{U}$  target, thus serving as an equivalent non-neutron producing target well-suited for noise estimates. The rate of the detection of coincident events in the neutron ToF range while using the Al target was 3% that of the  $^{238}\text{U}$  target. Thus, 3% of coincident events used in the determination of n-n angular correlations in  $^{238}\text{U}$  can be attributed to noise.

607 contain no detected neutrons.

608 While  $nn_{dp}(\theta_{nn})$  and  $nn_{acc}(\theta_{nn})$  are proportional,  
609  $nn_{acc}(\theta_{nn})$  is not equal to  $nn_{dp}(\theta_{nn})$ , because there are,  
610 on average, more detected neutrons per pulse-pair than  
611 per pulse. As the following analysis shows,  $nn_{acc}(\theta_{nn}) =$   
612  $\frac{1}{2}nn_{dp}(\theta_{nn})$ , under the condition that  $nn_{acc}(\theta_{nn})$  is nor-  
613 malized to the number of pulses and  $nn_{dp}(\theta_{nn})$  to the  
614 number of pulse-pairs considered. When looking at single  
615 pulses, the probability of there being a detected uncorre-  
616 lated n-n pair is denoted by  $P_{sp}^{\text{n-n}}$ , and when looking at  
617 pulse-pairs, by  $P_{dp}^{\text{n-n}}$ . Thus,  $P_{sp}^{\text{n-n}}$  and  $P_{dp}^{\text{n-n}}$  determine the  
618 relative rates of  $nn_{acc}(\theta_{nn})$  and  $nn_{dp}(\theta_{nn})$ , respectively.  
619 The statistics of the detected uncorrelated neu-  
620 trons per pulse is assumed to follow a Poisson distribu-  
621 tion, which describes the occurrence of independent ran-

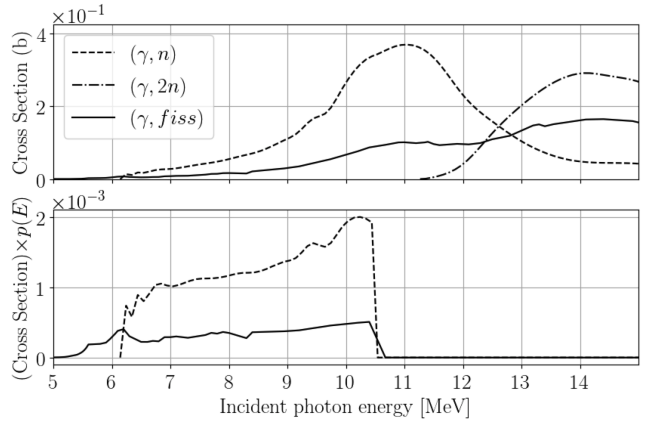


**FIG. 17:** (top) ENDF cross-sections of  $(\gamma, \text{fiss})$ , direct  $(\gamma, n)$ , and direct  $(\gamma, 2n)$ . (bottom) Cross-sections weighted by the simulated relative rate of bremsstrahlung photons that reach the target as a function of photon energy. The integrated cross-sections of  $(\gamma, n)$  is 5.5 times greater than for  $(\gamma, \text{fiss})$ . Assuming a  $\bar{\nu}$  of 2 neutrons/fission, the bremsstrahlung beam produces about 2.7 times more neutrons via  $(\gamma, n)$  than  $(\gamma, \text{fiss})$ .

622 dom events. Accordingly, the probability of the detection  
623 of  $k$  uncorrelated neutrons in a given pulse is

$$p(k) = \frac{e^{-\lambda} \lambda^k}{k!}, \quad (6)$$

624 where  $\lambda$  represents the mean number of uncorrelated de-  
625 tected neutrons per pulse. In principle,  $\lambda$  equals the total  
626 number of detected uncorrelated neutrons divided by the  
627 total number of pulses. Determination of  $\lambda$  cannot be  
628 done in practice, because one would need to know which  
629 pairs of detected neutrons are correlated. However, the  
630 largest possible value for  $\lambda$  is the total number of de-  
631 tected neutrons divided by the total number of pulses, as  
632 this quantity counts all detected neutrons, whether they  
633 are correlated or uncorrelated. For this work, that places  
634 an upper bound on  $\lambda$  of  $5.5 \times 10^{-3}$  detected uncorrelated  
635 neutrons per pulse, which is small enough to truncate all  
636 terms beyond the leading term in the following analysis.

637 Because  $P_{sp}^{\text{n-n}}$  represents the probability of the detec-  
638 tion of two uncorrelated neutrons in a single pulse,  $P_{sp}^{\text{n-n}}$   
639 is equal to  $p(2)$ , as per Eq. 6. Thus,

$$\begin{aligned} P_{sp}^{\text{n-n}} &= \frac{e^{-\lambda} \lambda^2}{2!} \\ &\approx \frac{\lambda^2}{2} + \mathcal{O}(\lambda^3). \end{aligned} \quad (7)$$

640 When considering the case of  $P_{dp}^{\text{n-n}}$ , recall that, in  
641 this case, uncorrelated n-n pairs are formed by exam-  
642 ining pulse-pairs. Here, an uncorrelated n-n pair occurs  
643 when there is a detected neutron in both pulses. Because  
644 all terms beyond the leading term are being truncated,  
645 pulse-pairs in which one or both of the pulses comprise  
646 two or more detected neutrons do not need to be con-

sidered. Thus,  $P_{dp}^{n-n}$  is equal to the probability of there being exactly one detected neutron in each pulse, which is the square of the probability of there being exactly one detected neutron in a single pulse, namely,  $p(1)^2$ . Thus, again using Eq. 6,

$$\begin{aligned} P_{dp}^{n-n} &= (e^{-\lambda}\lambda)^2 \\ &\approx \lambda^2 + \mathcal{O}(\lambda^3). \end{aligned} \quad (8)$$

Because  $P_{dp}^{n-n}$  and  $P_{sp}^{n-n}$  determine the relative rates of  $nn_{dp}(\theta_{nn})$  and  $nn_{acc}(\theta_{nn})$ , respectively, and because the two distributions have the same shape, from Eq.'s (8) and (7), it follows that

$$nn_{acc}(\theta_{nn}) = \frac{1}{2}nn_{dp}(\theta_{nn}). \quad (9)$$

Finally, from Eq.'s 9 and 5, the distribution of solely correlated n-n pairs can be recovered from the raw measurement as follows

$$nn_{corr}(\theta_{nn}) = nn_{raw}(\theta_{nn}) - \frac{1}{2}nn_{dp}(\theta_{nn}). \quad (10)$$

## 559 V. POTENTIAL SOURCES OF ERROR

### 600 A. Correlated versus uncorrelated n-n energy 601 distribution

In order to effectively minimize the dependence of the result on detector geometry/efficiency, the numerator and denominator of Eq. 4 must comprise neutron pairs with a similar energy distribution. Note that accidental coincident neutrons from  $(\gamma, n)$  are completely removed from  $nn_{corr}(\theta)$ , the numerator in Eq. 4, by the subtraction of accidental coincidences, but are not removed from the denominator,  $nn_{uncorr}(\theta)$ . This is the reason for using only pulse-pairs that have two events in each pulse when determining the uncorrelated neutron distribution. Doing so increases the selection of neutrons from fission as opposed to  $(\gamma, n)$ .

When examining differences between the neutron energy distributions in  $nn_{corr}(\theta)$  and  $nn_{uncorr}(\theta)$ , it is important to consider how the energies of both neutrons forming n-n pairs vary together, or, in other words, their joint energy distribution. Figure 18 shows the ratio between the rates for correlated and uncorrelated n-n pairs of various binned energies. The effect that these discrepancies in energy distribution have on the final result can be examined by applying a weighting factor to each event in  $nn_{uncorr}(\theta)$  such that a recalculation of the result in Fig. 18 produces a flat curve. A comparison of the angular correlation with and without the application of these weighting factors to uncorrelated n-n events is seen in Fig. 19. The resulting weighted distribution is identical within experimental uncertainties to the unweighted distribution, suggesting that differences in the energy distributions of  $nn_{corr}(\theta)$  and  $nn_{uncorr}(\theta)$  do not significantly

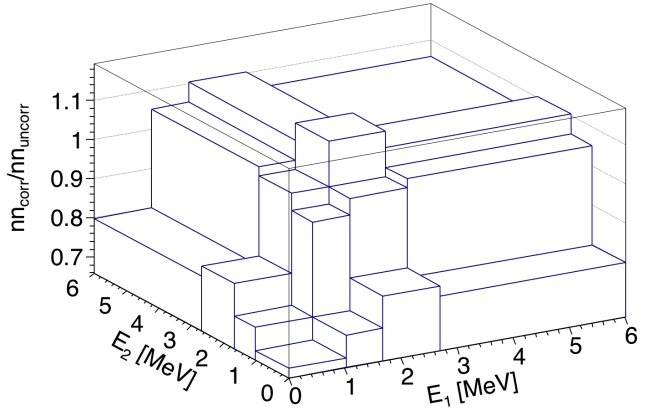


**FIG. 18:** The z-axis represents the ratio between the correlated and uncorrelated rates of binned n-n energies. The energy bins are chosen such that each contains an equal number of events, or 1/16th of the total events.

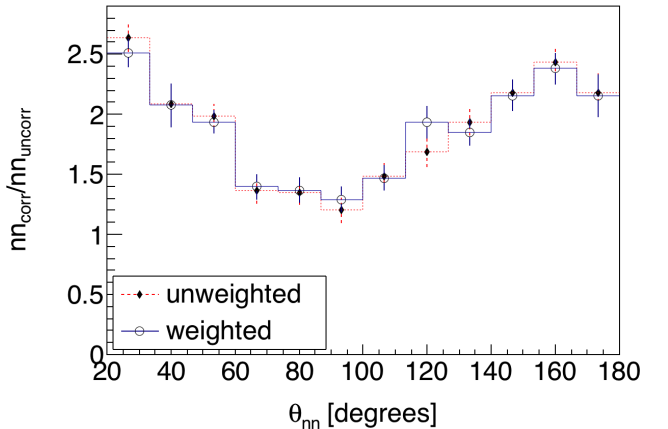


**FIG. 19:** Each uncorrelated n-n event can be weighted such that the weighted histograms of the joint n-n energy distributions of correlated and uncorrelated n-n pairs are equal. Comparison of the calculated angular correlation results, with and without such weighting factors applied to all uncorrelated n-n events, illustrates that any effects due to the discrepancies in the joint energy distributions of correlated and uncorrelated n-n pairs are negligible.

affect the present measurement.

### 694 B. Detector Cross-talk

*Cross-talk* occurs when, after a particle is detected once, the same particle, by any means, causes a detection to be registered in a different detector. For example, upon detection, a particle may undergo elastic scattering and then travel into another detector where it is detected again, or, it may produce secondary particles that are detected. The two coincident detections of a cross-talk event are causally correlated, and thus they have the potential to contaminate the signal from correlated fission neutrons. If both detections occur during the ToF range

705 typical for fission neutrons, then the cross-talk event can-  
 706 not be distinguished from the detection of two correlated  
 707 neutrons.

708 Recent works that measured the n-n angular correla-  
 709 tions in the spontaneous fission of  $^{252}\text{Cf}$  and  $^{240}\text{Pu}$  [8, 12]  
 710 addressed this effect by using an MCNP-PoLiMi simula-  
 711 tion to estimate and then subtract cross-talk from their  
 712 measurements. In this work, the issue of cross-talk is  
 713 approached differently by employing the use of detector  
 714 shielding aimed at reducing cross-talk to a negligible rate.  
 715 By using shielding to reduce cross-talk, this measurement  
 716 is less dependent on the details of the models used by  
 717 MCNP-PoLiMi to simulate neutron transport and detec-  
 718 tion. MCNP-PoLiMi simulations are used in this work  
 719 only to verify that the effect of cross-talk is negligible.

720 The scintillators used here are much larger than those  
 721 used in similar works, such as in Refs. [8, 12], allowing  
 722 them to be placed much farther from the fission source  
 723 without causing a detrimental loss in coincidence rates.  
 724 An increase in the distance between the detectors and the  
 725 fission source makes this measurement less subject to to  
 726 angular uncertainty, which depends directly on the un-  
 727 certainty in the position of a detected particle due to, for  
 728 example, the scattering of neutrons from detector shield-  
 729 ing. For this reason, larger amounts of shielding can be  
 730 used without concern of introducing large errors.

731 Furthermore, the geometry of the neutron detection  
 732 system makes it kinematically impossible for a neutron  
 733 to undergo a single scattering event with a proton in one  
 734 detector, which is the basis for scintillation, and then  
 735 travel directly into another detector with enough kinetic  
 736 energy to be detected a second time. For this reason,  
 737 upon being detected, a neutron must scatter from one or  
 738 more intermediate nuclei, such as lead or carbon, in or-  
 739 der for it to reach another detector with enough energy  
 740 to be detected again. This fact follows from the con-  
 741 servation of energy and momentum. In order to support  
 742 the claim that the design of the neutron detection system  
 743 reduced cross-talk to negligible rates, a detailed MCNP-  
 744 PoLiMi [15] simulation was performed in which a built-in  
 745  $^{252}\text{Cf}$  source is positioned at the center of a model of the  
 746 neutron detection system.

### 747 1. Simulation of Detector Cross-talk

748 The cross-talk simulation included all scintillators,  
 749 shielding, detector supporting structures, and the con-  
 750 crete walls surrounding the experimental cell. MCNP-  
 751 PoLiMi's built-in  $^{252}\text{Cf}$  spontaneous fission source was  
 752 used, which emits neutrons with the correct corre-  
 753 lations and multiplicities according to previous measure-  
 754 ments. Detector response was modeled using a program  
 755 included with the MCNP-PoLiMi distribution called MP-  
 756 Post [16]. The model is based on the MeV electron equiv-  
 757 alent (MeVee) light output produced by particles as they  
 758 undergo collisions with carbon and hydrogen within or-  
 759 ganic plastic scintillators. A minimum deposited energy

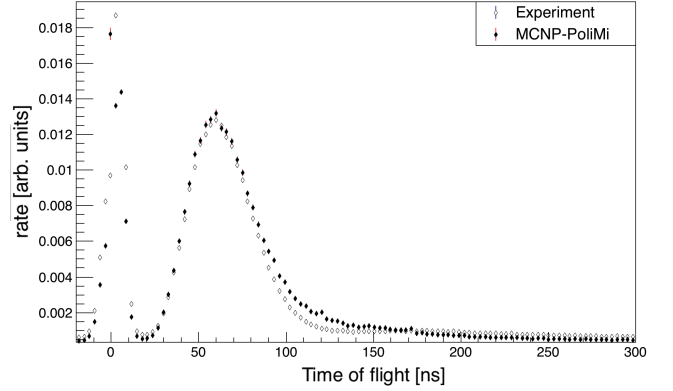


**FIG. 20:** Measured *versus* simulated ToF spectrum from the SF of  $^{252}\text{Cf}$ . The simulation used the detector response model outlined in ref [16]. The simulated and measured curves are normalized in order to facilitate comparison.

760 of 0.4 MeV (equivalent to 0.05 MeVee for neutrons) was  
 761 assumed for detectable particles, which was chosen be-  
 762 cause the neutron detection system exhibited a sharp de-  
 763 cline in detection efficiency for neutrons below 0.4 MeV.

764 For neutron collisions with hydrogen, the light output  
 765 in MeVee, denoted  $L$ , is calculated by the following em-  
 766 pirically derived formula [16]

$$L = 0.0364\Delta E_n^2 + 0.125\Delta E_n,$$

767 where  $\Delta E_n$  is equal to the loss in the kinetic energy of the  
 768 neutron due to the collision. Neutron interactions with  
 769 carbon are assumed to generate a small light output of

$$L = 0.02\Delta E_n.$$

770 As seen in Fig. 20, this model of the detection process  
 771 produces a ToF spectrum for the SF of  $^{252}\text{Cf}$  that shows  
 772 good agreement with the measurement for neutrons with  
 773 a ToF less than 100 ns and fair agreement for neutrons  
 774 with a ToF greater than 100 ns.

776 Figure 21 shows the distribution of cross-talk events  
 777 and true n-n coincidences as a function of reconstructed  
 778 opening angle. It is worth noting that, according to this  
 779 simulation, the effect of cross-talk is not only small, but  
 780 is also distributed over a wide range of n-n opening angles  
 781 rather than being concentrated around 0 degrees as one  
 782 might expect. Angles greater than 125 degrees are not  
 783 shown in Fig. 21 because cross-talk events at large an-  
 784 gles can be readily identified in analysis due to the large  
 785 amount of time required for a neutron to travel these  
 786 distances. The simulation was initially performed with 5  
 787 cm of lead shielding placed behind the scintillators, and  
 788 the number of cross-talk events accounted for 11% of the  
 789 total coincident neutron events. This value fell to 3%  
 790 when polyethylene was used instead of lead, motivating  
 791 the placement of 10 cm of polyethylene behind the de-  
 792 tectors instead of lead.

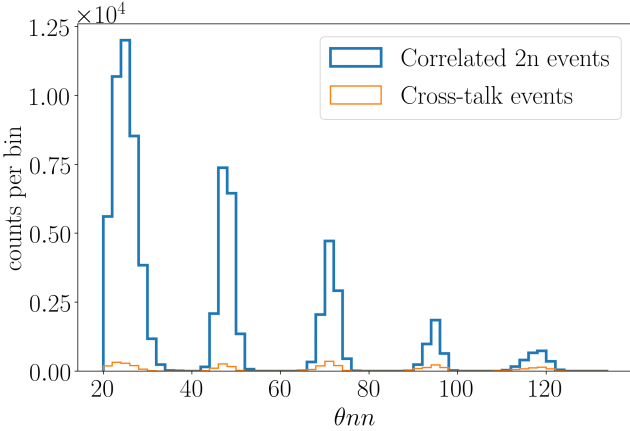


**FIG. 21:** MCNP-PoLiMi simulation of the number of cross-talk events *versus* correlated n-n events as a function of reconstructed opening angle. Cross-talk accounted for 3% of total events. Simulated cross-talk events do not occur primarily at small angles, but are instead spread out over a wide range of angles. Any cross-talk occurring at angles larger than  $125^\circ$  will be removed from the experimental data by the cuts applied to neutron ToF.

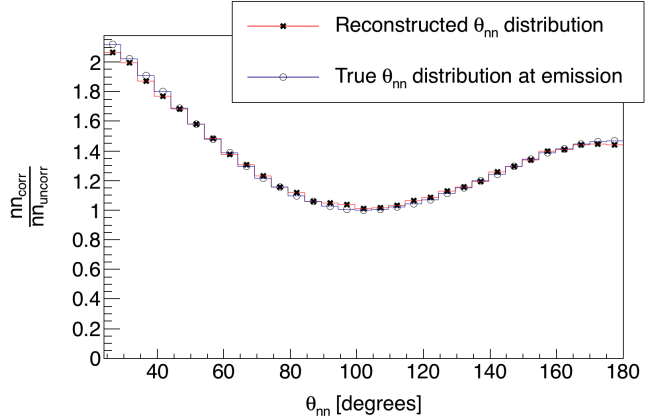


**FIG. 22:** MCNP-PoLiMi simulation of correlated  $^{252}\text{Cf}$  neutrons sampled uniformly throughout a  $0.05 \times 2 \times 4 \text{ cm}^3$  U-238 target. The slight difference between the curves is due solely to the elastic scattering of neutrons within the target, since detector physics was not simulated. In the reconstructed  $\theta_{nn}$  distribution ( $\star$ ), only neutrons which enter a physical volume at which a detector was located during the experiment are counted. The true  $\theta_{nn}$  distribution at the moment of emission is also plotted ( $\circ$ ).

### 794 C. Neutron Scattering within the Target

795 A potential source of error in opening angle measurements is the scattering of emitted neutrons as they tra-  
796 versed the fission target. This is cause for concern because  
797 when neutrons scatter from heavy nuclides such as  $^{238}\text{U}$ ,  
798 they are likely to be deflected at large angles resulting in  
799 n-n opening angles that do not reflect the true underlying  
800 fission kinematics. The effect that this has on this work  
801 is assessed by MCNP simulations. In summary, for 6% of  
802 n-n pairs, at least one neutron out of the two scatters be-  
803 fore exiting the target, according to the simulation. This  
804 effect does not have a large influence on the measured  
805  $\theta_{nn}$  distribution according to the simulation data shown  
806 in Fig. 22.

807 The rate of elastic scattering is affected by the size  
808 and shape of the target. A thin strip is the ideal target  
809 shape regarding the rate of neutron elastic scattering per  
810 unit of total target volume. See Fig. 23 for the simulated  
811 elastic scattering rates for both thin strip and cylindrical  
812 shaped targets. The simulation indicates that the rate of  
813 elastic scattering in cylindrical targets is about a factor  
814 of two times greater than in thin strip targets with the  
815 same volume.

816 The target's dimensions are small enough that the  
817 rate of photon absorption, and thus photo-neutron pro-  
818 duction, is virtually uniform throughout the entire tar-  
819 get volume. An MCNP-PoLiMi simulation was used  
820 to generate  $^{252}\text{Cf}$  spontaneous fission events uniformly  
821 throughout the target. The SF of  $^{252}\text{Cf}$  is used instead  
822 of the photofission of  $^{238}\text{U}$  because of the current lack  
823 of photofission models, however, the underlying fission  
824 kinematics are, broadly speaking, the same for the SF of  
825  $^{252}\text{Cf}$  and the photofission of  $^{238}\text{U}$ . Thus, the two pro-

826 cesses have similar n-n correlations.

827 Section VI B discusses the observation of an unex-  
828 pected drop in correlation around  $180^\circ$  n-n opening an-  
829 gle for the photofission of  $^{238}\text{U}$ , as seen in Figs. 24 and  
830 25. This motivated a second simulation regarding elastic  
831 scattering which examined whether this decrease in the  
832 correlation around  $180^\circ$  opening angles reflects the un-  
833 derlying physics of the fission process. In particular, note  
834 that throughout these measurements, the target was con-  
835 tinuously rotated once per 8 seconds. This means that for  
836 the determination of the uncorrelated opening angle dis-  
837 tribution, the trajectories of the two neutrons were taken  
838 from two different pulses in which the target was at a dif-  
839 ferent orientation for each of them. Additionally, each of  
840 the neutrons likely originated from different regions of the  
841 target volume. On the other hand, for the same-pulse,  
842 correlated neutron measurement, the target was in the  
843 same orientation and the two neutrons were generated  
844 at the same position in the target. For these reasons,  
845 the rates of neutron scattering within the target are not  
846 necessarily equal for the same-pulse and different-pulse  
847 cases. As such, we investigated whether these differences  
848 could cause this apparent decrease in the opening angle  
849 distribution near  $180^\circ$ .

850 Using the correlated  $^{252}\text{Cf}$  SF source built-in to  
851 MCNP-PoLiMi, the opening angle distribution of neu-  
852 trons at the moment of emission, labeled *true* in Fig. 22,  
853 were compared to that of the neutrons after they have es-  
854 caped the target, labeled *reconstructed* in Fig. 22. The lo-  
855 cation of fission events were sampled uniformly through-  
856 out the target's volume. The analysis employs the same  
857 technique outlined in section IV A, in which a correlated  
858 neutron distribution is divided by an uncorrelated neu-

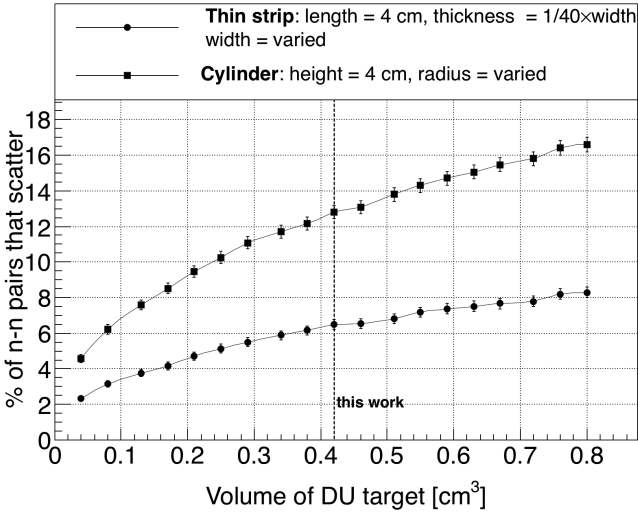


**FIG. 23:** Result of an MCNP simulation in which n-n pairs, with energies sampled from a typical watt fission spectrum, were generated uniformly throughout the volume of DU targets. The y-axis is the rate of opening angle contamination due to the scattering of, within the DU target in which they were produced, either one or both of a pair of neutrons. The lack of symmetry of a thin strip target can be removed by slowly rotating the target around the vertical axis during data acquisition, making it the optimal target geometry for the minimization of the rate of neutron scattering. The target used in this work had a length of 4 cm, a width of 2 cm, and a thickness of 0.05 cm.

tron distribution. The correlated neutron distribution is formed by pairing neutrons emitted during the same fission, and the uncorrelated distribution by the pairing of neutrons emitted during different fissions. In order to account for the effect of a rotating target on the trajectories of neutrons from different pulses, the coordinate system was rotated about the vertical axis accordingly for different fission events. The result from this simulation suggests that the rotating  $0.05 \times 2 \times 4 \text{ cm}^3$  U-238 target does not, due to neutron scattering, result in a measurable departure from the true n-n opening angle distribution.

## VI. RESULTS

### A. Comparisons with FREYA

The n-n opening angle correlation is calculated using the methods outlined in Sec. IV, in which a correlated neutron yield is divided by an uncorrelated yield. The results are compared with output from FREYA [17] (Fission Reaction Event Yield Algorithm), which was developed by the collaborative efforts of researchers from Lawrence Berkeley National Laboratory, Lawrence Livermore National Laboratory, Los Alamos National Laboratory, and University of Michigan Nuclear Engineering, and has been included in MCNP beginning with version

### 6.2.

The most recent release of FREYA (version 2.0.3) does not model photofission directly, but instead uses a neutron-induced fission model as an *ad hoc* photofission model [18]. Modeling photofission in this manner is a crude approximation, unbacked by experimental verification. Nonetheless, due to the current lack of accepted photofission models, the approximate model included in FREYA version 2.0.3 is compared with the results of the present work.

For a given nucleus with Z protons and A total nucleons, the code selects the neutron-induced fission model for a Z(A-1) nucleus, and chooses an incident neutron energy such that the compound ZA nucleus will have, relative to ZA's ground state, an excitation energy that is equal to the energy of the would-be incident photon.

When using FREYA to model photofission in this work, all model parameters, such as level density and partition parameters, were set to their default values for neutron-induced fission. FREYA was configured to use the fission fragment mass distribution,  $Y(A)$ , and the average total kinetic energy,  $\langle \text{TKE} \rangle(A)$ , from the  $^{238}\text{U}$  photofission measurements described in Ref. [19].

The measured  $\theta_{nn}$  distribution from the photofission of  $^{238}\text{U}$  and the SF of  $^{252}\text{Cf}$  are presented with the following two different types of cuts applied to the energies of neutrons in coincidence: in Figs. 24 ( $^{238}\text{U}$ ) and 26 ( $^{252}\text{Cf}$ ), a minimum energy threshold is applied to both neutrons, and in Figs. 25 ( $^{238}\text{U}$ ) and 27 ( $^{252}\text{Cf}$ ), the energy of both neutrons are required to fall within a specified range

In each of Figs. 24 through 27, the data are reported using two representations: the classic histogram and the kernel density estimate (KDE). When using a histogram to estimate a continuous distribution from the relatively small number of data points obtained in this work, one faces the following dilemma: small bin-widths lead to large uncertainties that are dependent on the chosen bin-width, while large bin-widths obscure potentially useful information. This problem is mitigated by the use of a KDE. A KDE is a method for estimating a continuous probability distribution from a finite set of sampled data points. The kernel was chosen to be the measurement errors in opening angle as determined by a study using coincident photons from a  $^{60}\text{Co}$  source, which was placed at different locations along a detector. The measurement errors in  $\theta_{nn}$  are well-described by a gaussian with a standard deviation of  $6^\circ$ . Mathematical details of the KDE method used in this work are outlined in Ref. [20]. The error bands seen in Figs. 24 through 27 correspond to 68% confidence intervals.

Plotted alongside each measurement is the result of a FREYA simulation. For the measurement of  $^{238}\text{U}$  photofission, there were a total of 2,952 n-n coincident events after the subtraction of accidentals, and for the SF of  $^{252}\text{Cf}$ , there were 21,882.

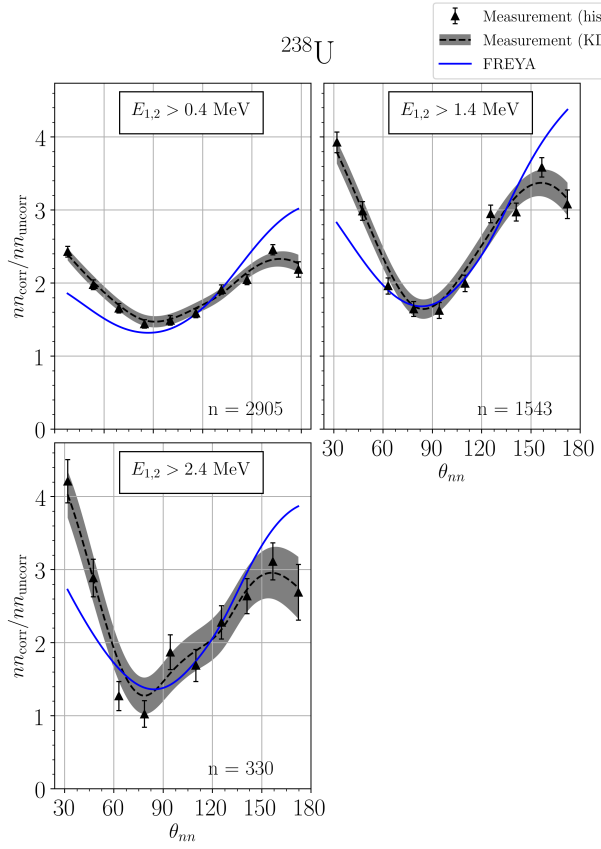


**FIG. 24:**  $\theta_{nn}$  distribution with minimum neutron energy cuts applied. The number of events contributing to each plot,  $n$ , is shown. Note that the bottom plots of this figure and Fig. 25 are identical.

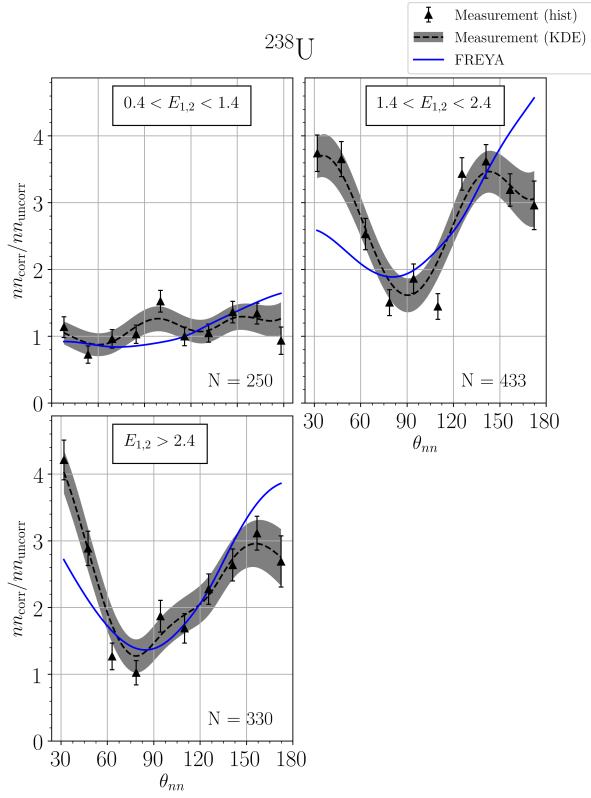


**FIG. 25:**  $\theta_{nn}$  distribution with cuts requiring that the energy of both coincident neutrons be within the specified range. The number of events contributing to each plot,  $n$ , is shown. Note that the bottom plots of this figure and Fig. 24 are identical.

## 941 B. Anomalous emission at large opening angles

942 While the results reported in the previous section are  
943 consistent with the effect of the kinematic focusing of the  
944 neutrons due to the recoil of the fission fragments, the  
945 data for U-238 show a statistically significant decrease  
946 in the n-n opening angle correlation in the region from  
947 about  $165^\circ$  to  $180^\circ$ , which can be seen in Figs. 14 and  
948 30, as well as in Figs. 24 and 25. The effect is particularly  
949 strong for the neutron energy cuts being applied in the  
950 upper right plots of both Figs. 24 and 25. A comparison  
951 of the observed decrease after  $160^\circ$  degrees with the null  
952 hypothesis that the true distribution remains constant af-  
953 ter  $160^\circ$  degrees yields a p-value of 0.01. This indicates a  
954 1% probability of obtaining data as compatible with the  
955 above hypothesis as the data we observed. This is a fea-  
956 ture which does not seem to universally appear in either  
957 neutron-induced or spontaneous fission. A similar but  
958 less pronounced effect appears in the results reported in  
959 Ref. [11] for the thermal neutron-induced fission of  $^{233}\text{U}$   
960 and  $^{235}\text{U}$ , but not for the spontaneous fission of  $^{252}\text{Cf}$  or  
961 the neutron-induced fission of  $^{239}\text{Pu}$ . The prominence of  
962 this effect observed in the present work may be a charac-

963 teristic feature of the photofission of the even-even  $^{238}\text{U}$   
964 nucleus.

965 Interesting effects are also seen when plotting neutron  
966 correlation *versus* energy for several different opening an-  
967 gle cuts. Fig. 28 top shows the correlation when a min-  
968 imum threshold is applied to the absolute difference in  
969 the energies of coincident n-n pairs. Note that a suppres-  
970 sion of correlated emission for large opening angles only  
971 occurs in n-n pairs that have a large difference in energy,  
972 as indicated by Fig. 28 top.

973 While a definitive explanation of these results would be  
974 greatly aided by detailed modeling studies, These data  
975 are consistent with two possible explanations relating to  
976 the unique feature of the asymmetric angular emission  
977 of fission fragments in photofission. First, the neutrons  
978 may indeed be emitted isotropically in the rest frame of  
979 the fission fragment, but one fragment essentially shad-  
980 ows the neutrons emitted from the other fragment, either  
981 through absorption or scattering, leading to a decrease in  
982 emission along the fission axis. The decrease in corre-  
983 lation at  $\theta_{nn}$ 's greater than  $170^\circ$  for n-n pairs with a large  
984 energy difference, as seen in Fig. 28 top, is consistent with  
985 the proposed shadowing mechanism for the case of neu-  
986 tron pairs emitted along the fission axis from the same

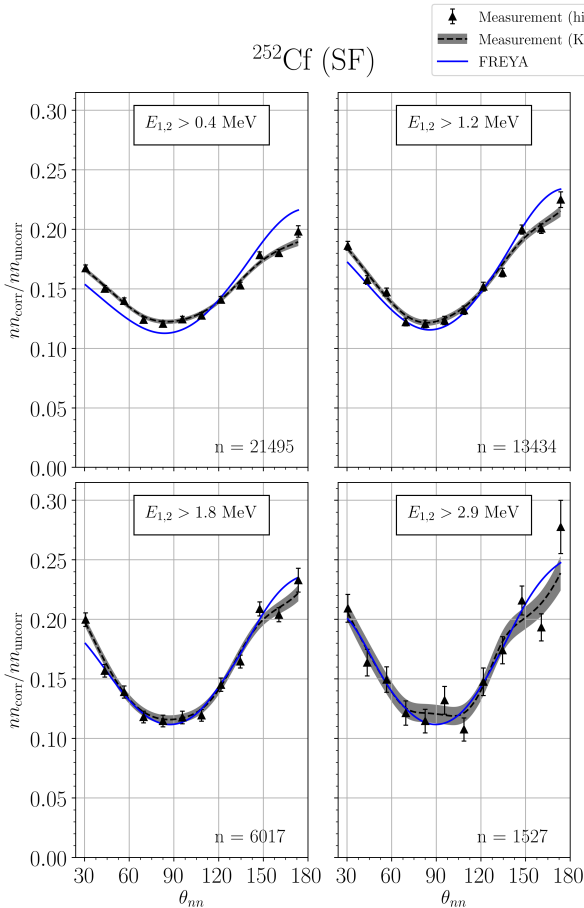


**FIG. 26:**  $\theta_{nn}$  distribution with minimum neutron energy cuts applied. The number of events contributing to each plot,  $n$ , is shown. Note that the lower right plots of this figure and Fig. 27 are identical.

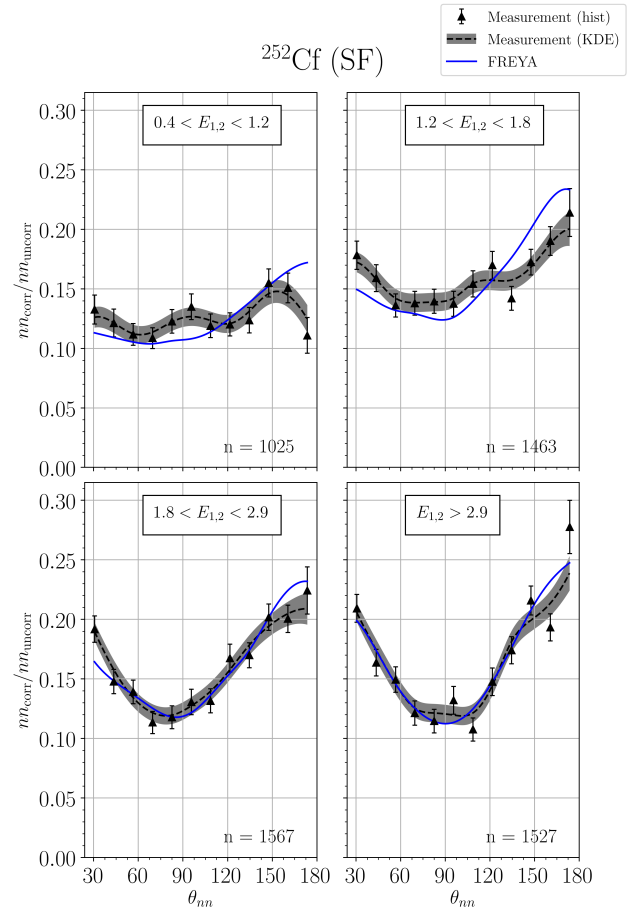


**FIG. 27:**  $\theta_{nn}$  distribution with cuts requiring that the energy of both coincident neutrons be within the specified range. The number of events contributing to each plot,  $n$ , is shown. Note that the lower right plots of this figure and Fig. 26 are identical.

fragment, because one neutron receives a boost to high energy from the fragment and the other a boost to low energy. Similarly, the decrease in correlation at  $\theta_{nn}$  greater than  $170^\circ$  for n-n pairs in which both neutrons have relatively low energy, as seen in Fig. 28 middle, is consistent for the case of neutron pairs emitted along the fission axis from opposite fragments, because both neutrons receive a boost to lower energy. Second, there is, due to unknown reasons, a decrease in neutron emission along the fission axis. If it is the former case, then this effect has the potential to shed light on the time dependence of neutron emission, since shadowing would likely depend on the fission fragment separation. A definitive interpretation of this decreased n-n correlation for large opening angles in photofission requires further study.

As previously discussed in section IC, photofission differs from spontaneous and neutron induced fission in that the fission fragments for the photon-induced reaction exhibit an asymmetry in their angle of emission, with the most likely orientation of the fission axis lying perpendicular to the direction of the incident photon. With this in mind, the following series of angular cuts were made on the data. Figure 29 shows the distributions of absolute opening angles of the n-n events for three different cuts on the value of the n-n opening angle. For n-n opening angles between  $120^\circ$  and  $160^\circ$ , there is an increased preponderance of both neutrons being emitted around  $90^\circ$ , consistent with the interpretation of kinematic focusing of neutrons coming from fission fragments which are themselves being emitted preferentially at  $90^\circ$ . However, in the opening angle region where the n-n correlation is reduced, from about  $160^\circ$  to  $180^\circ$ , this feature is

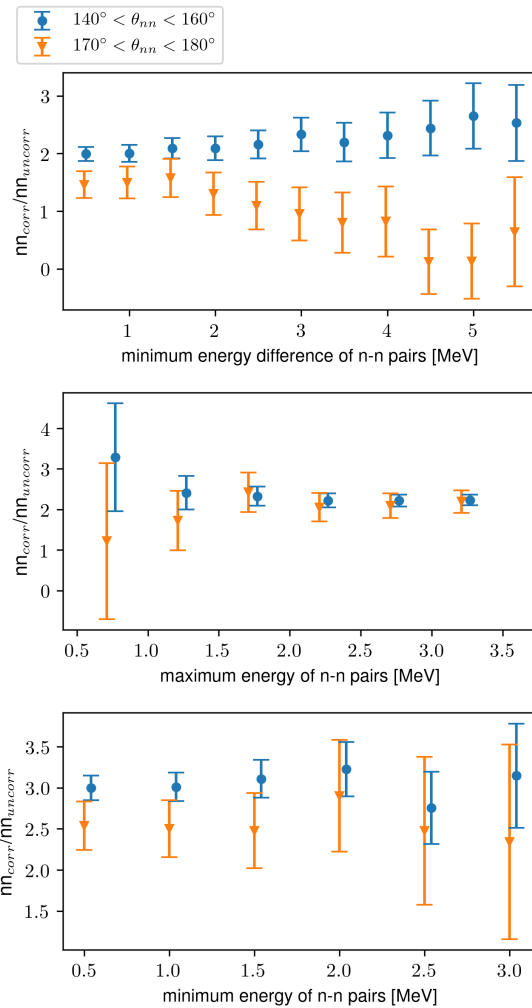


**FIG. 28:** From the photofission of  $^{238}\text{U}$ . The x-axes of each plot corresponds to various cuts applied to the energies of the two neutrons forming coincident n-n pairs. (top) cuts are the minimum absolute difference between the energies of both coincident neutrons. (middle) cuts are a maximum energy threshold of both coincident neutrons. (bottom) cuts are a minimum energy threshold of both coincident neutrons.

<sup>1021</sup> less prominent.

<sup>1022</sup> Furthermore, if one plots the opening angle distribu-  
<sup>1023</sup> tions for the case in which at least one neutron is emitted  
<sup>1024</sup> perpendicular to the incident photon *versus* the case in  
<sup>1025</sup> which neither neutron is emitted perpendicular to the  
<sup>1026</sup> incident photon (Fig. 30), one sees distinct differences.  
<sup>1027</sup> The fact that there are overall differences is not surpris-  
<sup>1028</sup> ing, because in one case (Fig. 30 solid line) at least one  
<sup>1029</sup> neutron preferentially receives a kinematic boost from a  
<sup>1030</sup> fission fragment and in the other case (Fig. 30 dotted  
<sup>1031</sup> line) neither neutron does. However, the fact that the  
<sup>1032</sup> n-n correlation is reduced at  $180^\circ$  in opening angle when  
<sup>1033</sup> at least one of the neutrons is emitted along the preferred  
<sup>1034</sup> fission axis is unexpected. This is a feature which does  
<sup>1043</sup> not seem to appear in most previous measurements of  
<sup>1044</sup> either neutron-induced or spontaneous fission, as well as  
<sup>1045</sup> bremsstrahlung photons produced via a low duty factor,

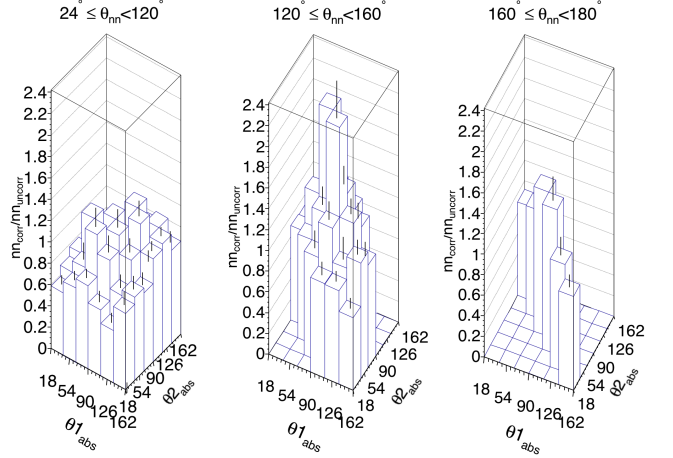


**FIG. 29:** Visualization of the correlation between the angles of each neutron with respect to the incident photon beam, denoted by  $\theta_{1\text{abs}}$  and  $\theta_{2\text{abs}}$ . Empty bins exist because of intrinsic geometrical phase-space. Data taken from measurements of  $^{238}\text{U}$  photofission.

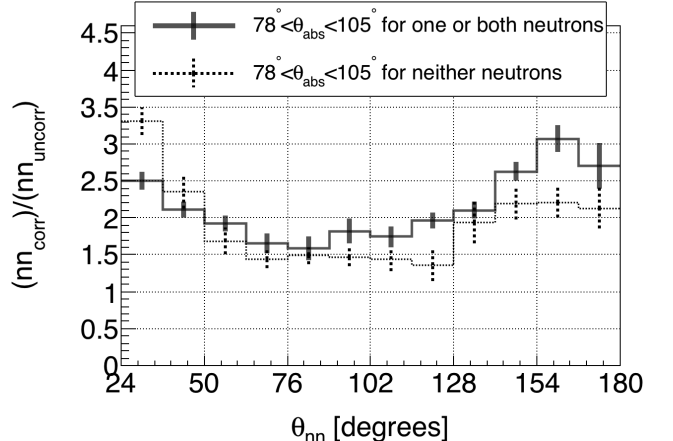


**FIG. 30:** Requiring that at least one of the coincident neutrons be emitted nearly perpendicular to the photon beam (solid line) produces an opening angle distribution that is different from that produced when it is required that both neutrons are emitted nearly parallel to the photon beam (dotted line). Data taken from measurements of  $^{238}\text{U}$  photofission.

<sup>1037</sup> our present measurement on spontaneous fission. The  
<sup>1038</sup> attribution of this effect to the geometric coverage of the  
<sup>1039</sup> neutron detection system or to neutron elastic scatter-  
<sup>1040</sup> ing within the target was ruled out using simulations, as  
<sup>1041</sup> discussed in section V C.

## VII. CONCLUDING REMARKS

Neutron-neutron angular correlations in the photofis-  
<sup>1044</sup> sion of  $^{238}\text{U}$  were measured using 10.5 MeV end-point  
<sup>1045</sup> bremsstrahlung photons produced via a low duty factor,

pulsed linear electron accelerator. The measured angular correlations reflect the underlying back-to-back nature of the fission fragments. The method of analysis used a single set of experimental data to produce an opening angle distribution of correlated and uncorrelated neutron pairs. A ratio is taken between these two sets to provide a self-contained result of angular correlations, in that the result is independent of neutron detector efficiencies. Neutron-neutron angular correlation measurements were also made using neutrons from the spontaneous fission of  $^{252}\text{Cf}$  and show good agreement with previous measurements.

offer two possible explanations for this effect. First, the neutrons may indeed be emitted isotropically in the rest frame of the fission fragment, but one fragment essentially shadows the neutrons emitted from the other fragment, either through absorption or scattering. Second, that there is, due to unknown reasons, a decrease in neutron emission along the fission axis. While these measurements do not provide a definitive interpretation of this decreased n-n correlation for large opening angles in photofission, further study may have the potential to shed light on the time evolution of neutron emission in photofission.

Measured n-n opening angle distributions from the photofission of  $^{238}\text{U}$  are in great disagreement with the *ad hoc* photofission model included in FREYA version 2.0.3. This is expected, because the model is only a crude approximation which uses a neutron-induced model to approximate photofission. The present measurement will be useful for fine-tuning photofission models included in future releases of FREYA.

In addition, we report for the first time a pronounced anomaly in the n-n angular distributions from photofission, in which the rate of neutron emission at opening angles near  $180^\circ$  is diminished, resulting in a local maximum at about  $160^\circ$  instead of the expected  $180^\circ$ . We

measurements do not provide a definitive interpretation of this decreased n-n correlation for large opening angles in photofission, further study may have the potential to shed light on the time evolution of neutron emission in photofission.

It is our hope that these first measurements of n-n correlations in photofission will provide the impetus for future modeling of the fundamental physics of fission.

## VIII. ACKNOWLEDGMENTS

This work has been supported by the National Nuclear Security Administration, grant DE-NA002488. We wish to thank the staff of the Idaho Accelerator Center for their assistance in this work. We also wish to acknowledge early contributions to this work by our friend and colleague the late David V. Jordan of the Pacific Northwest National Laboratory.

- 
- [1] J. T. Caldwell, E. J. Dowdy, R. A. Alvarez, B. L. Berman, and P. Meyer. Experimental determination of photofission neutron multiplicities for  $^{235}\text{U}$ ,  $^{236}\text{U}$ ,  $^{238}\text{U}$ , and  $^{232}\text{Th}$  using monoenergetic photons. *Nuclear Science and Engineering*, 73(2):153–163, 1980.
  - [2] G. A. Petrov. Current status of the search for scission neutrons in fission and estimation of their main characteristics. *AIP Conference Proceedings*, 798(1):205–212, 2005.
  - [3] Harry R. Bowman, Stanley G. Thompson, J. C. D. Milton, and Wladyslaw J. Swiatecki. Velocity and angular distributions of prompt neutrons from spontaneous fission of  $\text{Cf}^{252}$ . *Phys. Rev.*, 126:2120–2136, Jun 1962.
  - [4] C. Budtz-Jørgensen and H.-H. Knitter. Simultaneous investigation of fission fragments and neutrons in  $^{252}\text{Cf}$  (SF). *Nuclear Physics A*, 490(2):307 – 328, 1988.
  - [5] P. Talou, R. Vogt, J. Randrup, M. E. Rising, S. A. Pozzi, J. Verbeke, M. T. Andrews, S. D. Clarke, P. Jaffke, M. Jandel, T. Kawano, M. J. Marcath, K. Meierbachtol, L. Nakae, G. Rusev, A. Sood, I. Stetcu, and C. Walker. Correlated prompt fission data in transport simulations. *The European Physical Journal A*, 54(1):9, Jan 2018.
  - [6] S. Debenedetti, J. E. Francis, W. M. Preston, and T. W. Bonner. Angular dependence of coincidences between fission neutrons. *Phys. Rev.*, 74:1645–1650, Dec 1948.
  - [7] J. S. Pringle and F. D. Brooks. Angular correlation of neutrons from spontaneous fission of  $^{252}\text{Cf}$ . *Phys. Rev. Lett.*, 35:1563–1566, Dec 1975.
  - [8] J. M. Verbeke, L. F. Nakae, and R. Vogt. Neutron-neutron angular correlations in spontaneous fission of  $^{252}\text{Cf}$  and  $^{240}\text{Pu}$ . *Phys. Rev. C*, 97:044601, Apr 2018.
  - [9] Sara A. Pozzi, Brian Wieger, Andreas Enqvist, Shaun D. Clarke, Marek Flaska, Matthew Marcath, Edward Larsen, Robert C. Haight, and Enrico Padovani. Correlated neutron emissions from  $^{252}\text{Cf}$ . *Nuclear Science and Engineering*, 178(2):250–260, 2014.
  - [10] A. M. Gagarski, I. S. Guseva, V. E. Sokolov, G. V. Val'ski, G. A. Petrov, D. O. Krinitin, D. V. Nikolaev, T. A. Zavarukhina, and V. I. Petrova. Neutron-neutron angular correlations in spontaneous fission of  $^{252}\text{Cf}$ . *Bulletin of the Russian Academy of Sciences, Physics*, 72:773–777, July 2008.
  - [11] V. E. Sokolov and G. A. Petrov. Investigation of the angular dependences of neutron-neutron coincidences from  $^{252}\text{Cf}$ ,  $^{235}\text{U}$ ,  $^{233}\text{U}$  and  $^{239}\text{Pu}$  fission in search of scission neutrons. *Proc. XVIII Internat. Seminar on Interaction of Neutrons with Nuclei (ISSIN-18)*, pages 108–118, 2010.
  - [12] Matthew J. Marcath, Tony H. Shin, Shaun D. Clarke, Paolo Peerani, and Sara A. Pozzi. Neutron angular distribution in plutonium-240 spontaneous fission. *Nuclear Instruments and Methods in Physics Research, Section A: Accelerators, Spectrometers, Detectors and Associated Equipment*, 830:163–169, 9 2016.
  - [13] S Nair, D B Gayther, B H Patrick, and E M Bowey. Fission-neutron and fragment angular distributions from threshold photofission of  $^{232}\text{Th}$  and  $^{238}\text{U}$ . *Journal of Physics G: Nuclear Physics*, 3(7):965, 1977.
  - [14] Jefferson Lab. CODA 2.6, 2015.
  - [15] Sara A Pozzi, Enrico Padovani, and Marzio Marseguerra. MCNP-PoliMi: a Monte-Carlo code for correlation measurements. *Nuclear Instruments and Methods in Physics Research Section A: Accelerators, Spectrometers, Detec-*

- 1156      *tors and Associated Equipment*, 513(3):550 – 558, 2003. 1168  
1157 [16] Eric C. Miller, Shaun D. Clarke, Marek Flaska, Sara 1169  
1158 A. Pozzi, and Enrico Padovani. MCNPX-PoliMi post- 1170  
1159 processing algorithm for detector response simulations. 1171  
1160 *JNMM, Journal of the Institute of Nuclear Materials 1172 Management*, 40(2):34–41, 12 2012. 1173  
1161  
1162 [17] Lawrence Berkeley National LaboratoryLawrence Liver- 1174  
1163 more National LaboratoryLos Almost National Labora- 1175  
1164 toryUniversity of Michigan Nuclear Engineering. *FREYA 1176 2.0.3*, 2016. 1177  
1165 [18] S. D. Clarke, B. M. Wieger, A. Enqvist, R. Vogt, J. Ran- 1178  
1166 drup, R. C. Haight, H. Y. Lee, B. A. Perdue, E. Kwan, 1179  
1167
- C. Y. Wu, R. A. Henderson, and S. A. Pozzi. Measurement of the energy and multiplicity distributions of neutrons from the photofission of  $^{235}\text{U}$ . *Phys. Rev. C*, 95:064612, Jun 2017.  
[19] Krishichayan, M. Bhike, A. P. Tonchev, and W. Tornow. Fission product yield measurements using monoenergetic photon beams. In *European Physical Journal Web of Conferences*, volume 146 of *European Physical Journal Web of Conferences*, page 04018, September 2017.  
[20] Kyle Cranmer. Kernel estimation in high-energy physics. *Computer Physics Communications*, 136(3):198–207, 2001.